nature biomedical engineering

ARTICLES

https://doi.org/10.1038/s41551-020-0568-z

Check for updates

Intravital three-dimensional bioprinting

Anna Urciuolo[1,2,3], Ilaria Poli[4], Luca Brandolino[1,2], Paolo Raffa[2,3], Valentina Scattolini[2,3], Cecilia Laterza[1,2], Giovanni G. Giobbe[5], Elisa Zambaiti[3], Giulia Selmin[5], Michael Magnussen[5], Laura Brigo[2], Paolo De Coppi[5,6], Stefano Salmaso[7], Monica Giomo[1] and Nicola Elvassore[1,2,5,8]✉

Fabrication of three-dimensional (3D) structures and functional tissues directly in live animals would enable minimally invasive surgical techniques for organ repair or reconstruction. Here, we show that 3D cell-laden photosensitive polymer hydrogels can be bioprinted across and within tissues of live mice, using bio-orthogonal two-photon cycloaddition and crosslinking of the polymers at wavelengths longer than 850 nm. Such intravital 3D bioprinting—which does not create by-products and takes advantage of commonly available multiphoton microscopes for the accurate positioning and orientation of the bioprinted structures into specific anatomical sites—enables the fabrication of complex structures inside tissues of live mice, including the dermis, skeletal muscle and brain. We also show that intravital 3D bioprinting of donor-muscle-derived stem cells under the epimysium of hindlimb muscle in mice leads to the de novo formation of myofibres in the mice. Intravital 3D bioprinting could serve as an in vivo alternative to conventional bioprinting.

Three-dimensional printing is an additive process in which successive layers of materials are structured to generate 3D shapes. The technology is being applied to enable rapid prototyping and manufacturing in industry, as well as production of personalized consumer products[1,2]. Advanced systems have recently implemented layer-by-layer precise positioning of biomaterials, predominantly hydrogels, as well as biochemicals and live cells into complex 3D functional tissues, thereby progressing from 3D printing to 3D bioprinting[3–6].

Three-dimensional bioprinting aims to replicate the composition, mechanical properties and 3D architecture of biological tissues and/or organs for a large spectrum of biomedical applications. These include the generation of complex in vitro 3D models for drug discovery or biological studies and the development of implantable functional living human constructs (biomaterials combined with cells) suitable for the restoration of tissue and/or organ function[3–6]. For clinical applications, 3D live constructs are either incubated in vitro for maturation before implantation or 3D bioprinted and then implanted in vivo[3–8] using surgical procedures. Recently reported in situ 3D bioprinting has been limited to damaged areas of external and accessible loci such as skin[9,10] or sites previously exposed by surgical procedure, such as bone[11] and cartilage[12]. Conventional bioprinting approaches require direct access to printing sites and freedom to move the bioprinting head along *x*, *y* and *z* axes, precluding internal modifications of pre-existing 3D structures without affecting the integrity of the structures of interest.

However, injectable materials used as delivery vehicles hold great promise for improvement of therapeutic efficacy for functional recovery of diseased or injured tissues and organs, including stem cell-based therapies[13], with a minimally invasive procedure. An injectable hydrogel is the preferred type of material for stem cell transplantation due to its potential to mimic the native stem cell microenvironment[14–16]. A variety of crosslinking strategies have been developed to form hydrogel structures in internal regions of tissues: (1) physical crosslinking, which includes ionic crosslinking and stimuli-responsive crosslinking (such as responses to temperature and pH change); (2) chemical crosslinking, which includes enzymatic, radical or click chemistry, and provides better control of the mechanical strength and degradation of the hydrogel, compared with physical crosslinking processes[13]. However, independently of the crosslinking strategy used, injectable hydrogels form an isotropic structure around the site of injection that cannot be controlled in terms of 3D shape and spatial organization.

In this work, we demonstrate the possibility of injecting photoactive polymers in live animals to directly fabricate in situ spatially controlled 3D constructs across and within tissues. We name this concept intravital 3D bioprinting (i3D bioprinting).

Compared with conventional 3D bioprinting, i3D bioprinting should be designed to confront and surpass additional hurdles, which are intrinsic to in vivo applications. These include (1) fabrication across tissues without inducing tissue damage or interfering with the pre-existing 3D tissue anatomical structures; (2) fabrication efficiency should not be affected by physiological tissue displacements such as those produced by the heartbeat or breathing of live animals; (3) accurate positioning and orientation of 3D bioprinted structures in tissues at site of interest to support cell function and/or tissue regeneration. Ideally, 3D bioprinting in a live animal would also require accurate pre-processing imaging for fine 3D mapping of the anatomical area in which the printed object needs to be manufactured, and post-processing analysis to effectively evaluate the positioning, orientation and accuracy of the printed object.

We overcome these hurdles by developing photosensitive biopolymers that can be used to fabricate hydrogels within and across solid matrices or tissues. These biopolymers can be crosslinked in vitro in presence of living cells or in a pre-mixed gel for controlling organoid shape and behaviour in 3D culture. Moreover, after a simple injection into the desired anatomical site (that is, in a tissue), photosensitive biopolymers can be photo-crosslinked in vivo to form a 3D

[1]Department of Industrial Engineering, University of Padova, Padova, Italy. [2]Veneto Institute of Molecular Medicine, Padova, Italy. [3]Department of Women's and Children's Health, University of Padova, Padova, Italy. [4]ONYEL Biotech, Padova, Italy. [5]University College London Great Ormond Street Institute of Child Health, London, UK. [6]Department of Specialist Paediatric and Neonatal Surgery, Great Ormond Street Hospital for Children, London, UK. [7]Department of Pharmaceutical and Pharmacological Science, University of Padova, Padova, Italy. [8]Shanghai Institute for Advanced Immunochemical Studies (SIAIS), ShanghaiTech University, Shanghai, China. ✉e-mail: n.elvassore@ucl.ac.uk

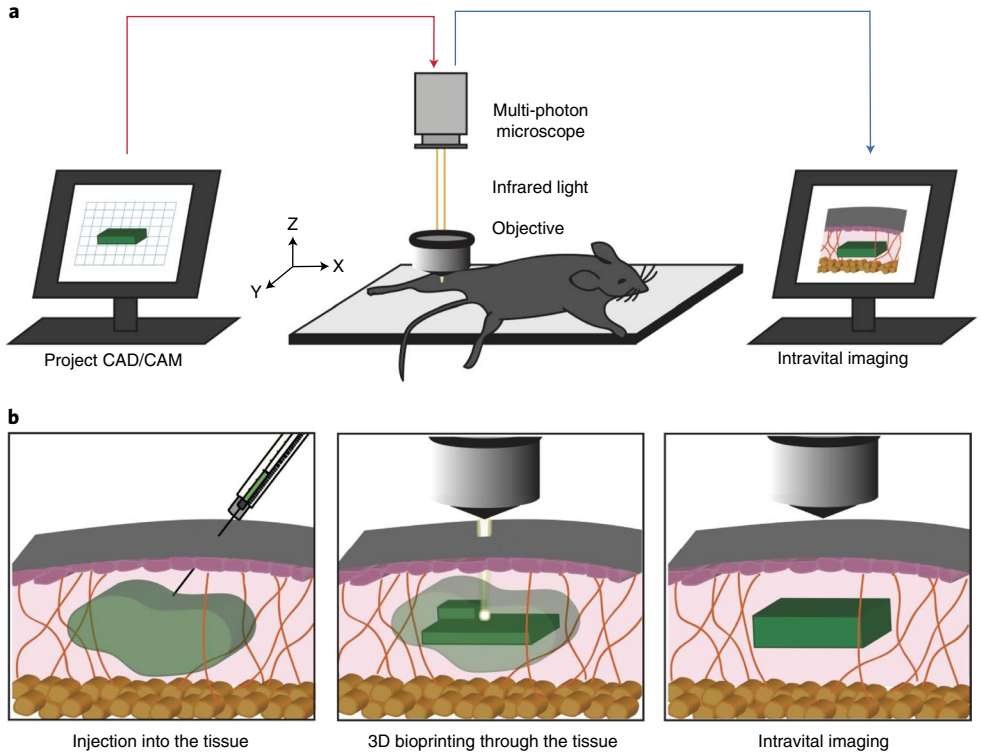

Fig. 1 | Intravital 3D bioprinting setup and in vivo application. a, i3D bioprinting requires a multiphoton microscope equipped with a motorized *xyz* stage and a femtosecond near-infrared tightly-focused pulsed laser emission. CAD, computer-aided design; CAM, computer-aided manufacture. **b**, i3D bioprinting is performed by injection of HCC–polymer solution into organs of live animals, fabrication of 3D hydrogel objects by two-photon excitation, and intravital imaging for hydrogel identification and in vivo analysis.

object by using near-infrared laser light associated with high-spatial resolution intravital multiphoton microscopy specifically designed for 3D-object fabrication (Fig. 1). This was accomplished by modifying biocompatible hydrophilic polymeric backbones with a hydrophobic, photoactive crosslinking group, which efficiently undergoes cycloaddition when two-photon excited at wavelengths longer than 850 nm. Owing to the selected wavelength range, tightly-focused femtosecond pulsed infrared laser light can penetrate through soft tissues[17], allowing 3D hydrogel photo-crosslinking inside and across tissues. We show that complex 3D hydrogels of branched polyethylene glycol (PEG) and gelatin are accurately fabricated into tissues of live mice such as dermis across epidermis, skeletal muscle across epimysium or brain across meninges. The 3D hydrogels show high biocompatibility and incorporation of a functional vascular network, which makes the i3D bioprinting a procedure suitable for clinical translation. Finally, we show that i3D bioprinting enables spatially-controlled donor-cell grafting and, importantly, supports the generation of newly formed myofibre bundles that are integrated with the functional vascular network of the host.

Results

Development of an infrared photo-crosslinking strategy. We initially developed a technology to enable photo-crosslinking of biopolymers into hydrogels by using laser wavelengths that allow deep tissue penetration[17] (wavelength (λ) > 800 nm). Accordingly, we selected coumarin derivatives as photosensitive crosslinking moieties for the end-functionalization of polymeric backbones. Coumarin derivatives have the potential to undergo [2 + 2] cycloaddition when exposed to single-photon ultraviolet–visible (UV–Vis) light[18–20] or under two-photon excitation at near-infrared light[18,21,22]. UV–Vis light photo-crosslinking can be performed to fabricate hydrogels in which coumarin derivatives have been used as photosensitive crosslinking moieties[23–26]. However, UV–Vis wavelengths are incompatible with tissue penetration[17]. A few applications have reported the use of coumarin derivatives for two-photon hydrogel degradation[25,26], but not for two-photon hydrogel fabrication. Coumarin derivatives were initially developed as fluorescent dyes to facilitate in vivo imaging of 3D coumarin-based hydrogel structures and their accurate positioning and orientation within live animals. Finally, coumarin-mediated cycloaddition offers the additional advantage of avoiding possible toxicity towards living tissues, on the basis of their radical- and photo-initiator-free chemistry[27].

We considered 58 known coumarin derivatives (Supplementary Table 1), and selected 8 of them for further characterization based on ring substituents that can influence their light-absorption properties and the chemistry for backbone conjugation (Fig. 2a, Supplementary Fig. 1 and Supplementary Table 2). Among them, 7-hydroxycoumarin-3-carboxylic acid (HCCA) was identified as an optimal candidate for i3D bioprinting application because it has an electron-donating substituent in the 7-position and an electron-withdrawing substituent in the 3-position, which promote a red-shift of the maximum absorption peak, thus offering an advantage in term of tissue permeability to laser light (Supplementary Figs. 1 and 2). Moreover, the presence of a carboxylic group allows the conjugation of HCCA to polymers such as linear PEG, branched PEG and gelatin (Fig. 2b and Supplementary Figs. 3 and 4; HCC–polymers), which are among the most common and best-characterized polymers used to fabricate biocompatible hydrogels[3–5]. The 7-Hydroxycoumarin-3-carboxylate (HCC)–PEG conjugates were characterized by ^{1}H-NMR and Fourier transform infrared (FT-IR) analysis, and size-exclusion chromatography confirmed HCC–gelatin conjugation (Supplementary Figs. 5–7). The conjugation degree was also quantified and absorbance spectra were analysed for all the HCC polymers (Supplementary Fig. 8).

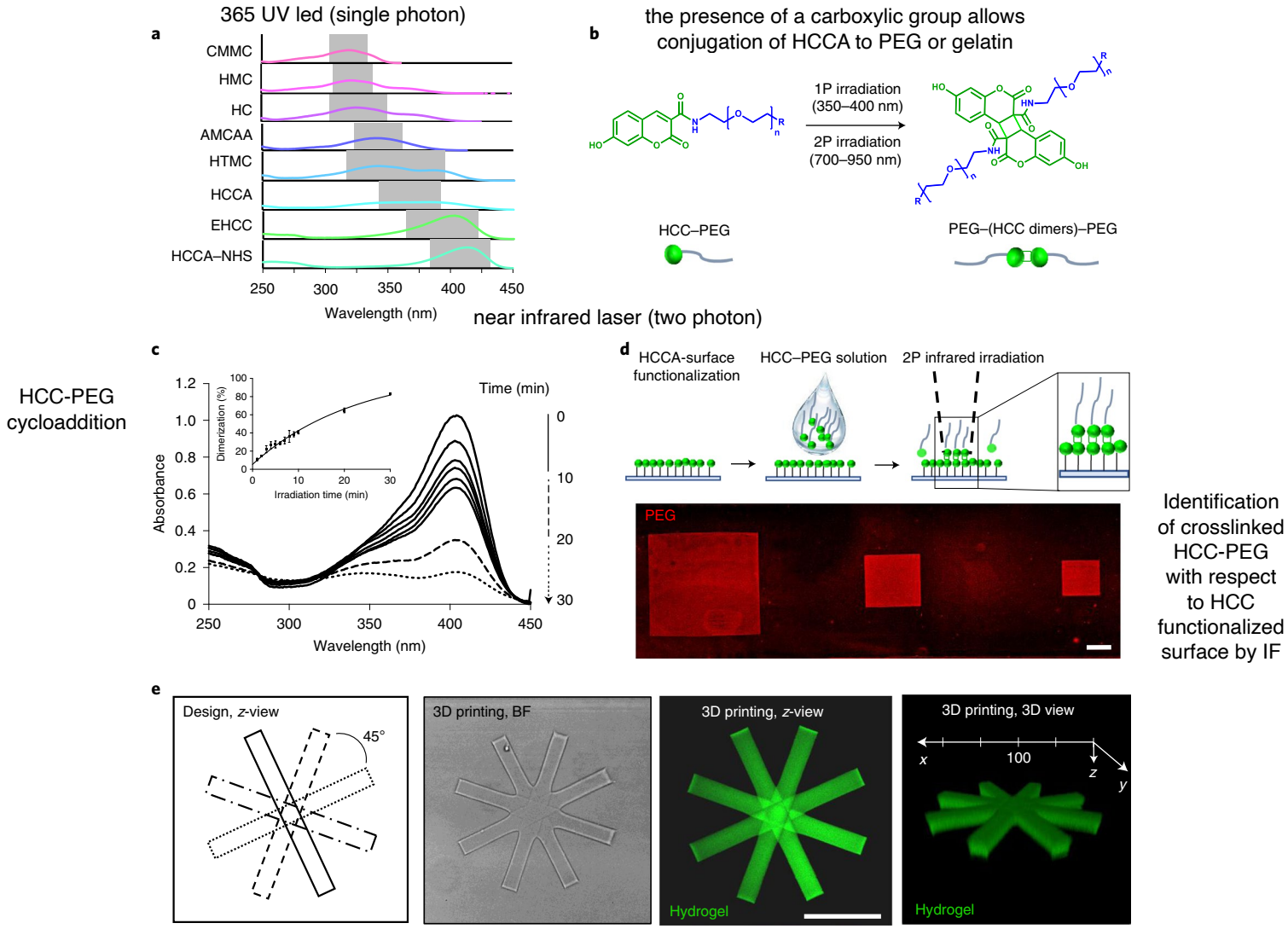

Fig. 2 | Development of injectable HCC-conjugated polymers for i3D bioprinting application. a, Absorption spectra of selected coumarin derivatives in PBS, pH 7.4. The grey rectangles highlight the maximum absorbance peaks. AMCAA, 7-amino-4-methyl-3-coumarinylacetic acid; CMMC, 7-carboxymethoxy-4-methylcoumarin; EHCC, ethyl 7-hydroxycoumarin-3-carboxylate; HC, 7-hydroxycoumarin; HMC, 7-hydroxy-4-methylcoumarin; HCCA-NHS, 7-hydroxycoumarin-3-carboxylic acid *N*-hydroxysuccinimidyl ester; HTMC, 7-hydroxy-4-(trifluoromethyl)coumarin. **b**, Illustration of HCC–PEG [2 + 2] cycloaddition reaction promoted by one-photon (1P) or two-photon (2P) irradiation. **c**, Absorbance spectra analysis showing HCC–PEG [2 + 2] cycloaddition after irradiation with single-photon light ($\lambda = 365$ nm) at different time points (2 to 10 min, continuous line; 20 min, broken line; 30 min, dotted line). The inset shows HCC–PEG dimerization degree with increasing irradiation time; Data are shown as mean ± s.d. of three independent replicates. **d**, Illustration of HCCA-surface functionalization and HCC–PEG two-photon near-infrared light-mediated cycloaddition ($\lambda = 800$ nm) in a defined area of excitation, performed by multiphoton microscopy. Identification of crosslinked HCC–PEG with respect to the HCC-functionalized surface was performed by PEG immunofluorescence (red). Scale bar, 200 μm. **e**, Design and fabrication of multiple 3D parallelepipeds of HCC–gelatin rotated by 45° around a mass centre placed on the same *z* plane. Representative bright-field (BF), confocal *z*-stack or 3D-volume reconstruction images of ten independent replicates are shown. $\Delta z = 20$ μm. Scale bars, 100 μm (*z*-view); in the 3D reconstruction, coordinates and 50 μm scale bar are shown. Specific bioprinting conditions are reported in Supplementary Table 3.

To test light-mediated cycloaddition of HCC–polymers, we initially used HCC-conjugated linear PEG (HCC–PEG) as a model. Single-photon excitation ($\lambda = 365$ nm) was able to induce HCC–PEG intermolecular cycloaddition in solution, resulting in dimerization of HCC–PEG, as shown by spectrophotometric analysis (Fig. 2c). The ability of HCCA to undergo cycloaddition was further confirmed by ^{1}H-NMR spectroscopy and electrospray-ionization mass spectrometry analysis of HCCA solution (Supplementary Figs. 9 and 10). Moreover, HCC underwent cycloaddition after two-photon excitation at a wavelength of 850 nm using a multiphoton laser-scanning microscope, as shown by the rapid 2D HCC–PEG patterning (approximately 10 s per 850 μm^2) onto HCCA-functionalized glass slides with high spatial precision (Fig. 2d).

Two-photon hydrogel fabrication. We then tested the possibility of assembling 3D hydrogel constructs by using branched PEG and gelatin polymers conjugated to HCCA and excited in a wide wavelength window. To screen for wavelengths (700 nm < λ < 1,000 nm) that allow two-photon crosslinking at mild laser power (0.7 mW), we found that hydrogels made of HCC–4-arm PEG, HCC–8-arm PEG and HCC–gelatin retain their shape after removal of the solution containing non-crosslinked polymers when fabricated at

700 nm < λ < 850 nm (Supplementary Fig. 11). By increasing laser power to 2 mW, HCC–8-arm PEG and HCC–gelatin can be crosslinked up to 900 nm (data not shown). Crosslinking is triggered only within the focal region (voxel) and the laser-scanning path of the multiphoton microscope provides spatial control of the reaction. Typically, *z*-stacks of regions of interest were two-photon excited. On the basis of the optical properties of the objective used, a *z*-spacing of 1 µm between adjacent planes was used. Thus, 3D structures with complex morphology could be easily fabricated by sequential addition of *z*-stacks of multiple regions of interest (Fig. 2e and Supplementary Fig. 12), including a readable barcode (Supplementary Fig. 12c), words (Supplementary Fig. 12c,d and Supplementary Video 1) or a hollow cube (Supplementary Fig. 12e and Supplementary Video 2). Figure 2e shows parallelepipeds that are rotated 45° in the same *z*-plane to form an asterisk.

Accuracy of 3D photo-crosslinking was further confirmed after fabrication of hydrogels by photo-crosslinking multiple *z* positions (Fig. 3a) or by assembling additively multiple parallel linear objects (Fig. 3b,c). The minimal line width (1.9 ± 0.2 µm) of fabricated linear objects (Fig. 3b) and the sub-micrometric resolution of the bioprinting (Fig. 3c) was achieved. Accordingly, a 3D single-line flower-shaped hydrogel of HCC–gelatin was fabricated using a computer drawing pad and a free line-scan program of the multiphoton microscope (Fig. 3d and Supplementary Video 3). Additionally, we tested the maximum 3D-object fabrication depth ($\Delta z \approx 2$ mm) that was attainable without changing printing parameters (scanning speed and laser power) (Fig. 3e and Supplementary Video 4).

Considering the intended in vivo application and taking in account the displacement due to animal respiratory movements and pulsed blood flow, we quantified an optimal writing time per single line that enables 3D hydrogel production with structural integrity (Fig. 3f). The optimal writing time of 1 ms per line was therefore used for the i3D bioprinting experiments; lower laser power does not trigger two-photon crosslinking, whereas higher power may induce heat damage. This efficient and fast bioprinting, able to preserve minimum feature dimension, is probably due to the threshold behaviour and nonlinear nature of multiphoton excitation[17] combined with highly efficient cycloaddition. In conventional two-photon polymerized hydrogels, a photo-initiator and possible co-initiator or sensitizer molecules activate a free-radical chemical crosslinking reaction through a diffusion-reaction mechanism[28,29]. In the case of coumarin-conjugated dipeptides (7-(diethylamino)-3-coumarin carboxylic acid), it was previously reported that cycloaddition is facilitated when coumarin moieties are in close proximity[23,24]. Coumarin-based polymers have been shown to generate micelles in aqueous solution[18]. In line with this, we observed by transmission electron microscopy that HCC–PEG forms nano-assemblies (Supplementary Fig. 13), supporting the idea that HCC polymers in aqueous solution can self-assemble into supramolecular structures, in which the HCC photoactive groups are brought in close proximity and are ready to undergo fast cycloaddition upon light excitation, resulting in efficient crosslinking reactions within a focused two-photon optical voxel.

Over the past decade, several reports have highlighted the paramount role of stiffness in regulation of cell behaviour[30,31]. Atomic force microscopy has been used to estimate the hydrogel elastic properties of hydrogels[32], which are strictly correlated with the hydrogel photo-crosslinking rate[33]. Interestingly, we were able to finely tune the stiffness of HCC-4-arm PEG or HCC–gelatin hydrogels over biological-matched ranges (1 kPa–20 kPa) by modulating the laser power (Fig. 3g). Indeed, multiphoton microscopes allow fine tuning of laser power[34], which in turn can modulate hydrogel photo-crosslinking rate[33], crosslinking density and, consequently, the hydrogel mechanical properties[32].

To better characterize hydrogel photo-crosslinking rate in multiple samples and larger volumes in conventional fabrication conditions, CMMC–4-arm PEG and CMMC–gelatin were specifically designed and produced to perform one-photon UV-mediated cycloaddition (Fig. 2a and Supplementary Figs. 14 and 15). The elastic modulus can be increased to asymptotic values by increasing the irradiation time, showing a sigmoidal temporal profile of elastic modulus that reached the polymer crosslinking saturation, independently of the polymeric backbone used (Fig. 3h). Interestingly, the modulation of elastic modulus of hydrogels obtained with one- and two-photon photo-crosslinking (with CMMC–gelatin and

Fig. 3 | Characterization of the photosensitive polymers. a, Design and representative confocal *z*-stack images of three independent replicates of HCC–gelatin objects fabricated at different *z* positions by using near-infrared laser pulses through a multiphoton microscope; total $\Delta z = 110$ µm. Three-dimensional-volume reconstruction reveals the volumetric position of the various objects; coordinates are shown. Scale bars, 100 µm. **b**, Top: representative phase-contrast image of 10 independent replicates of an isolated HCC–8-arm PEG structure fabricated as single scan, returning the minimum linewidth achievable by the multiphoton setup. $\Delta z = 20$ µm. Scale bar, 10 µm. Bottom: quantification of the minimum line width obtained. Data are shown as mean ± s.d. of three independent replicates. **c**, Multiple HCC–8-arm PEG structures of 6 independent replicates fabricated by near-infrared multiphoton laser pulses, showing the micrometre resolution of the multiphoton setup. $\Delta z = 20$ µm. Scale bar, 3 µm. **d**, Representative 3D reconstruction of 6 independent replicates of a HCC–gelatin single-line, flower-shaped hydrogel fabricated using the free line-scan program of the multiphoton microscope. $\Delta z = 30$ µm. Coordinates and 50 µm scale bar are shown. **e**, Representative 3D-volume reconstruction of 3 independent replicates of a HCC–8-arm PEG object showing the maximum fabrication depth reached using near-infrared laser pulses through a multiphoton microscope at fixed laser power (2 mW, before objective back-aperture) and wavelength (850 nm). $\Delta z = 2{,}000$ µm. Coordinates and 500 µm scale bar are shown. **f**, Left: representative confocal images of 3 independent replicates of HCC–gelatin hydrogels (autofluorescence, green) fabricated at different writing times (approximately 0.5, 1, 2 and 4 ms per line). Scale bar, 20 µm. Right: quantification of size (left *y*-axis, black) and autofluorescence intensity (right *y*-axis, blue) of HCC–gelatin hydrogel photo-crosslinked by near-infrared laser pulses associated with the multiphoton setup. Data are shown as mean ± s.d. of 3 independent replicates; one-way ANOVA with Tukey's multiple comparisons test. $^{**}P = 0.0028$; $^{***}P = 0.0003$ for 1 ms per line versus 0.5 ms per line. Interpolation curves are shown. a.u., arbitrary units. **g**, Young's modulus measured by atomic force microscopy of HCC–4-arm PEG (grey) and HCC–gelatin (black) hydrogels photo-crosslinked using near-infrared laser pulses through a multiphoton microscope with increasing laser power and fixed wavelength using multiphoton microscopy. Data are shown as mean ± s.d. of three or four independent replicates; one-way ANOVA with Tukey's multiple-comparisons test. $^{*}P = 0.0293$; $^{****}P < 0.001$. Specific fabrication conditions are reported in Supplementary Table 3. **h**, Young's modulus measured by atomic force microscopy of CMMC–4-arm PEG (CMMC–PEG; dashed grey line, left *y*-axis) or CMMC–gelatin (dashed black line, right *y*-axis) photo-crosslinked with a 365 nm UV LED at fixed working distance and increasing irradiation time. Interpolation curves are shown. Data are shown as mean ± s.d. of three independent replicates. Specific fabrication conditions are reported in Methods. **i**, Young's modulus measured by atomic force microscopy of HCC–gelatin (continuous line, left *y*-axis) or CMMC–gelatin (dashed line, right *y*-axis) at increasing polymer concentration. HCC–gelatin was photo-crosslinked with near-infrared laser pulses through a multiphoton microscope (two-photon) at fixed laser power (0.7 mW) and at 1 ms per line writing time. CMMC–gelatin was photo-crosslinked with a 365 nm UV LED at fixed working distance and 10 min irradiation time. Interpolation curves are reported. Data are shown as mean ± s.d. of three independent replicates. Specific fabrication conditions are reported in Methods or in Supplementary Table 3.

HCC–gelatin, respectively) by varying the polymer concentration showed remarkable similarity (Fig. 3i).

Together, these results demonstrated the ability to fabricate 3D hydrogels with precise 3D positioning, micrometre resolution and tunable physiological stiffness by using infrared light-mediated photo-crosslinking of HCC–polymer solutions.

In vitro biocompatibility. Given that hydrogels need to be fully biocompatible, we assessed the ability of HCC–gelatin to support in vitro culture of different cell types. Pre-assembled flat HCC–gelatin hydrogels ($\Delta z = 30\,\mu m$) supported adhesion and culture of human umbilical vein endothelial cells (HUVEC) cells (Supplementary Fig. 16a) and human embryonic stem cell (hESC)-derived neural stem cells (NSCs) (Fig. 4a and Supplementary Fig. 6b–d). Three days after seeding, hESC-derived NSCs showed expression of specific neural markers and absence of apoptosis when cultured on preassembled flat HCC–gelatin hydrogels (Fig. 4a and Supplementary Fig. 16e). Fibroblasts derived from green fluorescent protein (GFP)-expressing mice adhere efficiently to parallelepiped-shaped HCC–gelatin hydrogels characterized by different sizes (Δz up to 150 µm) and interspace (down to 10 µm) and change their morphology according to the 3D shape of fabricated hydrogels (Supplementary Fig. 17).

We further confirmed the biocompatibility of HCC–gelatin solution and of the photo-crosslinking strategy by using cell-laden HCC–gelatin solution. Six hours after hydrogel crosslinking, fibroblasts were viable and embedded within 3D hydrogel structures (Fig. 4b, Supplementary Fig. 18 and Supplementary Video 5).

Single scan: minimum linewidth achievable by the multiphoton setup

micrometre resolution

Maximum fabrication depth reached using near-infrared laser pulses through a multiphoton microscope at fixed laser power

Mechanical properties can be modulated by writing time

The elastic modulus can be increased to asymptotic values by increasing the irradiation time, reaching polymer crosslinking saturation, independently of the polymeric backbone

modulation of elastic modulus of hydrogels obtained with one- and two-photon photo-crosslinking is similar

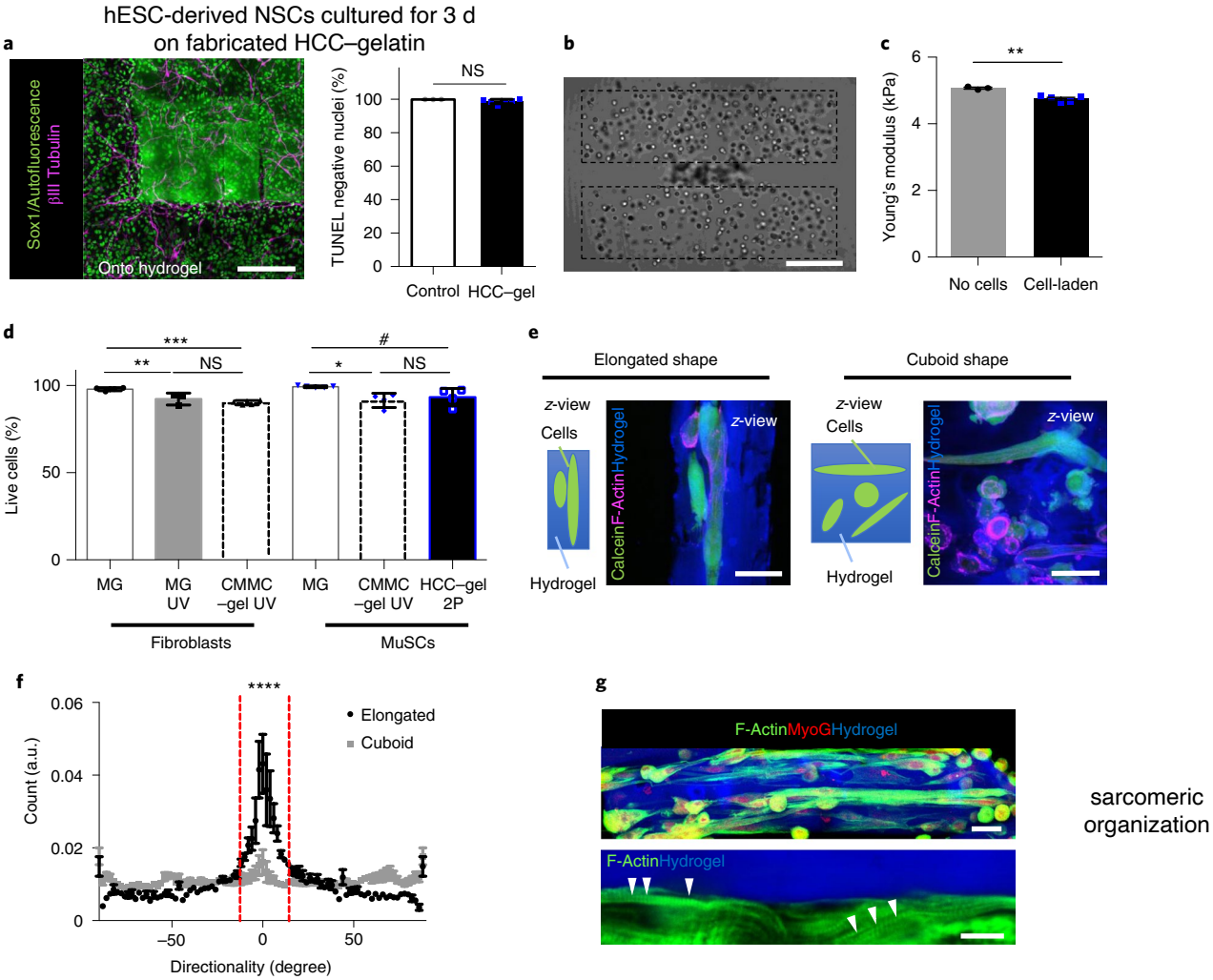

Fig. 4 | Three-dimensional objects of photosensitive gelatin hydrogels can be used for in vitro cell culture. a, Left: immunofluorescence analysis of Sox1 (green) and class III β-tubulin (magenta) of hESC-derived NSCs cultured for 3 d on fabricated HCC–gelatin (HCC–gel) hydrogel structures coated with poly-L-ornithine (on hydrogel). Scale bar, 200 μm. Right: quantification of non-apoptotic hESC-derived NSCs (TUNEL negative; expressed as percentage of total nuclei), cultured for 3 d on poly-L-ornithine and laminin coated glass (control) or on fabricated HCC–gelatin hydrogel structures coated with poly-L-ornithine (HCC–gel). Data are shown as mean ± s.d of three or six independent replicates; unequal variance Student's *t*-test; NS, not statistically significant. **b**, Representative image of a cell-laden HCC–gelatin structure 6 h after fabrication. Scale bar, 75 μm. **c**, Young's modulus of HCC–gelatin (no cells) or muscle fibroblast-laden HCC–gelatin (cell-laden) structures measured by atomic force microscopy photo-crosslinked at identical laser power (500 μW) and fixed wavelength (800 nm) using multiphoton microscopy. Data are shown as mean ± s.d. of 3 and 6 independent replicates; unequal variance Student's *t*-test; $^{**}P = 0.0016$. **d**, Survival of muscle fibroblast or mouse muscle-derived stem cells (MuSCs) suspended in Matrigel (MG), Matrigel exposed to UV (MG UV), CMMC-gelatin (CMMC-gel) crosslinked by UV light or HCC–gelatin two-photon-crosslinked and cultured for 48 h. Data are shown as mean ± s.d. of four independent replicates; one-way ANOVA with Tukey's multiple comparisons test. $^{\#}P = 0.049$; $^{*}P = 0.019$; $^{**}P = 0.0128$; $^{***}P < 0.001$. **e**, MuSCs orientation into a parallelepiped elongated- or cuboid-shaped HCC–gelatin cell-laden construct after 2 d of culture. Schematic illustration and representative fluorescence imaging showing *z*-stack reconstruction of MuSC-laden HCC–gelatin parallelepiped or cuboid constructs stained with calcein (green) and F-actin (magenta). Nuclei were stained with Hoechst (blue). Scale bars, 50 μm (cuboid) or 25 μm (elongated). **f**, Quantification of cell directionality of MuSCs 3D bioprinted into parallelepiped-shaped HCC–gelatin (elongated; black) or into cuboid-shaped HCC–gelatin (cuboid; grey) 2 d after printing. Data are shown as mean ± s.d. of eight independent replicates; two-way ANOVA with Sidak's multiple comparisons test. $^{****}P < 0.001$. **g**, Top: immunofluorescence of F-actin (green) and myogenin (MyoG, red) in myogenic cells after 10 d of cell culture. Bottom: higher magnification of F-actin (green) staining, in which sarcomeric organization is detectable (arrowhead). Hydrogel was revealed by autofluorescence (blue). Scale bars, 20 μm (top) and 10 μm (bottom). Specific bioprinting conditions are reported in Supplementary Table 4.

Notably, the elastic modulus of bioprinted structures was not strongly affected by the presence of cells (Young's modulus was reduced by about 6% in the presence of cells; Fig. 4c), suggesting that the two-photon crosslinking and hydrogel fabrication were not substantially affected by cells suspended in the HCC–gelatin solution. Next, we evaluated cell viability, comparing cell-laden constructs obtained with conventional single-photon hydrogel crosslinking ($\lambda = 365$ nm, single photon, CMMC–gelatin)[28,29] and those fabricated with two-photon bioprinting ($\lambda = 850$ nm, two-photon, HCC–gelatin) with irradiated-only ($\lambda = 365$ nm, Matrigel) or unirradiated (Matrigel) controls. Two days after 3D culture, cell viability was between 90–99% in all conditions (Fig. 4d). We observed that with our setup, single-photon irradiation time up to 3 min and two-photon bioprinting laser power up to 1 mW give good cell viability (as used in Fig. 4d), whereas increasing laser power was detrimental for viability (data not shown).

In vitro cell instructive hydrogel. Starting from these results, we then investigated whether the shape of 3D bioprinted cell-laden HCC–gelatin could provide specific topological cues. To investigate this, we used the ability of mouse muscle-derived stem cells (MuSC) to differentiate into myotubes and to adapt their morphology and orientation on the basis of microenvironment topology[35,36]. As confirmed by quantification of cell directionality, single-nucleated or polynucleated cells in elongated HCC–gelatin structures appeared oriented along the major axis of the 3D structures (Fig. 4e (left),f), whereas cells located in cuboid HCC–gelatin structures were randomly oriented (Fig. 4e (right),f).

Finally, to evaluate whether HCC–gelatin hydrogels were able to support cell culture for a longer time and maintain cell functionality, MuSCs were cultured on parallelepiped-shaped HCC–gelatin structures for 10 d. Microscopic analysis demonstrated that parallelepiped-shaped HCC–gelatin hydrogels support the formation of aligned multinucleated myotubes (Fig. 4g) that showed spontaneous contraction 5 d after induction of cell differentiation (Supplementary Video 6).

These results demonstrated that the photo-crosslinking of HCC-gelatin does not affect cell viability, is compatible with cell-laden 3D bioprinting, and supports stem cell differentiation and cellular function. It is worth underlining that our setup can be also used synergistically with conventional 3D bioprinting strategies[5].

In vitro bioprinting into pre-existing human organoid 3D culture. i3D bioprinting entails additional complexities: 3D bioprinting needs to be performed in anatomical sites of live animals, such as tissues, body cavities or extracellular matrix, which may include a variety of components of the interstitial space. We therefore tested the possibility of fabricating 3D-hydrogel objects in a pre-existing 3D matrix. We used Matrigel, a gel formed by a basement membrane equivalent that is widely used for 3D cultures of cells and organoids. A 50:50 HCC–gelatin:Matrigel mixture (v/v) was used to crosslink HCC–gelatin 3D structures of defined position and orientation within the gel. HCC–gelatin two-photon photo-crosslinking exhibited a bio-orthogonal reaction in pre-existing gel (Fig. 5a and Supplementary Video 7). When fabricated in pre-existing 3D Matrigel, hydrogel structures maintained their shape after Matrigel dissociation and, notably, showed comparable elastic modulus to hydrogel fabricated in the absence of Matrigel (Fig. 5b). Furthermore, HCC–gelatin–Matrigel 3D gels were able to support the viability and growth of human small intestinal organoids (hSIOs) (Supplementary Fig. 19)—which is a challenging type of culture to maintain[37]—while preserving the possibility of fabricating crosslinked objects within the gel. With this in mind, we fabricated 3D parallelepipeds that were accurately positioned and oriented relative to selected hSIOs within the 3D gel culture (Fig. 5c, Supplementary Fig. 20 and Supplementary Video 8). Subsequent analysis of such cultures is also possible, as shown by the intestinal epithelial marker ezrin and F-actin staining (Supplementary Fig. 20b). HCC–gelatin hydrogel cytocompatibility on hSIOs enclosed in the structures was demonstrated by live/dead assay performed after 2 d and 8 d of culture (Fig. 5d and Supplementary Fig. 21a).

Next, we investigated whether HCC–gelatin walls bioprinted in Matrigel and specifically positioned around individual hSIOs could affect their behaviour (Fig. 5c). hSIOs confined in an open square box (formed by four orthogonal walls) grew normally, and after few days of culture, touched and deformed HCC–gelatin hydrogel walls (Fig. 5e and Supplementary Fig. 21b). Between day 6 and day 8 of culture, hSIOs enclosed in HCC–gelatin-based hydrogel showed marked changes in morphology, which led to well-developed columnar epithelium (Fig. 5f). This morphology was characterized by thickening of the organoid wall, F-actin localization in the apical position and nuclei constriction in the basal domain, as quantified by the basal–apical distance ratio and the basal–apical axis (Fig. 5g–i). By contrast, hSIOs cultured in the same hydrogel composition but not in contact with HCC–gelatin structures did not show such morphological changes (Fig. 5f).

Interestingly, the basal localization of β4 integrin observed in hSIOs enclosed in HCC–gelatin structures (Fig. 5i) suggests that cell adhesion could be a possible mechanism involved in the observed phenotype. To dissect the contributions of extrinsic mechanical versus biochemical signals in triggering the organoid morphological changes, hSIOs cultured in Matrigel were enclosed in an open square box made of HCC-8-arm PEG-based hydrogel, which is known to have cell-repellent properties[8,38,39]. We show that HCC–8-arm PEG–Matrigel allowed hSIO survival and growth in culture (Fig. 5j). However, unlike the observations with HCC–gelatin, hSIOs enclosed in HCC–8-arm PEG-based hydrogel did not exhibit columnar epithelium after 8 d of culture, hydrogel deformation, actin apical localization or nuclei constriction (Fig. 5k,l). Instead, the morphology of the hSIOs reflects the 3D shape of the enclosed open box made by HCC–8-arm PEG-based hydrogel. Feret's angle quantification confirmed that only hSIOs enclosed by HCC–8-arm PEG acquired a cuboidal cystic structure after 6 d of culture, when compared with HCC–gelatin enclosed hSIOs (Fig. 5m).

Mechanical properties of synthetic hydrogels have a role in expansion and differentiation of mouse SIOs[40], whereas the effect of hydrogel stiffness on hSIO behaviour remains unclear. Our results suggest that the formation of hSIO columnar epithelium could be correlated to the biochemical composition of the hydrogel rather than its purely mechanical properties, since the HCC–gelatin and HCC–PEG had the same Young's modulus. It will be of interest to use this approach in future studies to investigate the cues that give rise to columnar epithelium in hSIOs.

In vivo hydrogel bioprinting. We next tested whether i3D printing is possible across tissues and inside tissues. Skin was identified as an optimal target organ in which to perform i3D printing without open surgery. The HCC–polymer solution was delivered locally by intra-dermal injection in wild-type or GFP$^+$ transgenic mice. Then, the HCC-polymer solution was exposed to focalized pulsed near-infrared laser light ($\lambda = 850$ nm) using a two-photon microscope (Fig. 6a). The mice were anaesthetized and subjected to i3D bioprinting in the skin. With this setup, we were able to efficiently fabricate isolated 3D objects inside the dermis (Fig. 6b and Supplementary Fig. 22a). In GFP$^+$ mice, by taking advantage of fluorescence of the host tissues, we could easily visualize both the fabricated objects inside the dermis and the integrity of the epidermis above the crosslinked hydrogel (Fig. 6b and Supplementary Video 9). The exact localization could be determined by the position of the hair bulb (Fig. 6b, arrow). The high compatibility of i3D bioprinting was further confirmed by the integrity of the skin after the procedure, which was similar to that of untreated tissue (Fig. 6b,c). Furthermore, as demonstrated in vitro, we showed that i3D bioprinting across epidermis enables the fabrication of 3D hydrogel structures with micrometre line width (Supplementary Fig. 22b), and the fabrication of inserts with a variety of morphologies thanks to the precise positioning (Supplementary Fig. 22a).

After demonstrating that i3D printing can be performed across epidermis without open surgery, we tested whether the technology was applicable to other tissues. Thus, we applied a surgical procedure to expose intact skeletal muscle or brain and HCC–polymer solutions were injected below the epimysium or meninges, respectively, and above the tissues of interest. Photosensitive solutions injected under the epimysium of skeletal muscle were photo-crosslinked to fabricate 3D hydrogels at the surface of muscle fibres without evident alteration of the overall muscle-fibre morphology and connective-tissue integrity (Fig. 6d,e, Supplementary Fig. 23 and Supplementary Video 10 and 11). Two-photon-crosslinked hydrogels were formed only in the region where the photo-reaction was

performed (Fig. 6f). Our experimental setup enables real-time imaging during and after i3D bioprinting, providing the possibility of triggering hydrogel crosslinking at a specific anatomical site; that is, on a single myofibre rather than on a bundle of myofibres. Given the natural anatomic patterning of myofibres, skeletal muscle was also used to verify the ability to fabricate i3D bioprinted hydrogels by precisely tuning their position and orientation. Multiple objects were fabricated in a parallel or orthogonal fashion when compared with their position and/or to myofibre orientation (Supplementary Fig. 24). The versatility of the fabrication protocol was further demonstrated by i3D bioprinting a HCC–gelatin hydrogel in the shape of the infinity symbol, using a design with input from a computer drawing to the free line-scan program of the multiphoton microscope (Supplementary Fig. 25).

Safe i3D bioprinting was also possible in the brain, which is a less robust tissue. A burr hole was drilled in the skull of mice to allow injection of HCC–polymer solution across the meninges, and subsequent hydrogel crosslinking was achieved by two-photon excitation with a multiphoton microscope (Fig. 6g). We observed correct maintenance of blood flow and no bleeding foci in the region where i3D bioprinting was performed (Fig. 6g and Supplementary Fig. 26a). Two-photon-crosslinked hydrogels surrounded and embedded the host vasculature network without damaging the vessels and preserved blood flow, as shown by labelled-dextran tracing (Fig. 6h and Supplementary Fig. 26b). These results further confirmed the biocompatibility of i3D bioprinting.

In vivo biocompatibility. To achieve the above results and effectively translate 3D hydrogel fabrication in vivo, we optimized laser power and writing time across tissues, balancing crosslinking efficiency, speed of 3D bioprinting (to reduce the effect of movements associated with breathing and cardiac beating) and heat-induced tissue damage. The optimal writing time (1 ms per line) was combined with the optimal laser power (1 mW) to obtain a stable hydrogel under epimysium without myofibre damage, as shown by the absence of heat-induced damage, myofibre contraction and cleavage of cell death-marker caspase 8[41,42] (Supplementary Fig. 27). Myofibre damage was observed only after two-photon irradiation with 3-fold increased laser power and about 17-fold increased time of irradiation per single confocal plane relative to the i3D bioprinting conditions (Supplementary Fig. 27).

Next, we investigated the biocompatibility of HCC–4-arm PEG and HCC–gelatin solution. HCC-4-arm PEG crosslinked hydrogels were preserved in vivo 4 d after i3D printing across epimysium, with no evident tissue damage at the site of two-photon crosslinking, as shown by image analysis (Supplementary Fig. 28a,b). Consistent with PEG biocompatibility studies[43], immunofluorescence analysis showed recruitment of macrophages to the site of hydrogel crosslinking, despite the absence of evident histological changes (Supplementary Fig. 28c,d). Since PEG hydrogels are cell repellent[8,38,39], and on the basis of previous in vitro results, we further investigated in vivo biocompatibility of our injectable HCC–gelatin hydrogels before challenging longer-term i3D printing in the presence of donor cells (i3D bioprinting). To demonstrate biocompatibility of HCC–gelatin, the polymeric solution was subcutaneously injected into wild-type mice and histological (haematoxylin and eosin and Masson trichrome) staining, TUNEL test and immunofluorescence staining for macrophages were performed after 4, 7 and 21 d. Compared with mice treated with PBS, no histological modification, cell apoptosis or macrophage infiltration was observed (Supplementary Fig. 29).

Finally, we aimed to show that i3D bioprinting could be effectively utilized in live animals to: (1) deliver cells in a spatially controlled manner; (2) enable precise cell grafting into a defined anatomical site; and (3) support appropriate structural organization of de novo tissues.

In vivo spatially controlled cell engraftment. We investigated whether i3D bioprinting could instruct spatial control of cell engraftment by first using HCC–gelatin laden with primary mCherry$^+$ fibroblasts, delivered across the epimysium in the hindlimb of isogeneic immunocompetent mice. Distinct freshly fabricated HCC–gelatin structures containing embedded mCherry$^+$ fibroblasts were located between the epimysium and skeletal muscle of host wild-type mice with the bioprinted structures (Supplementary Fig. 30a). Longer term studies were also performed to investigate

Fig. 5 | HCC–gelatin hydrogels can be fabricated into pre-existing 3D environments and are suitable for 3D in vitro hSIO culture. a, Left: representative images of objects fabricated in a drop of Matrigel. Scale bar, 400 μm. Right: 3D-volume reconstruction of the fabricated object in the gel; $\Delta z = 100$ μm. Coordinates and 100 μm scale bar are shown. **b**, Young's modulus of HCC–gelatin structures fabricated outside (black, no MG) or inside a Matrigel drop (white, into MG), measured by atomic force microscopy. Hydrogels were photo-crosslinked at identical laser power (800 μW) and fixed wavelength (800 nm) using multiphoton microscopy. Data are shown as mean ± s.d. of three independent replicates; unequal variance Student's *t*-test. **c**, Merged bright-field and fluorescent images showing hSIOs cultured in Matrigel, enclosed by HCC–gelatin structures after hydrogel photo-crosslinking. $\Delta z = 300$ μm. Scale bar, 50 μm. **d**, Representative bright-field and fluorescent images showing live (green, calcein-stained) and dead (red, ethidium homodimer-1-stained) cells in hSIO cultures 2 d after HCC–gelatin hydrogel two-photon crosslinking. Scale bar, 400 μm. The inset shows a higher magnification of the organoid enclosed in the HCC–gelatin hydrogel structure. Scale bar, 50 μm. $\Delta z = 300$ μm. Dashed lines indicate the hydrogel position. **e**, Representative images showing the morphology of a hSIO enclosed by HCC–gelatin 3D-printed structures after 3 d in culture. Hydrogel was deformed by the organoid. Dashed lines indicate the position of hydrogel walls. Scale bar, 50 μm. **f**, Confocal fluorescence image showing F-actin (magenta) organization in hSIOs after 8 d of cell culture. The green arrow indicates a hSIO enclosed in HCC–gelatin hydrogel (blue). The white arrow indicates a nearby organoid that was not enclosed by the hydrogel. Nuclei were stained with Hoechst (blue). Scale bar, 50 μm. **g**, Quantification of nuclear basal–apical (B–A) distance ratio of hSIOs in standard culture condition (control) or enclosed by Matrigel–HCC–gelatin hydrogels at day 3, 6 and 8 of cell culture. Data are shown as mean ± s.d. of 3 independent replicates; one-way ANOVA with Tukey's multiple comparisons test; $^{****}P < 0.0001$. **h**, Quantification of the major basal–apical axis length of hSIOs in standard culture conditions (control) or enclosed by Matrigel–HCC–gelatin hydrogels at day 6 and 8 of cell culture. Data are shown as mean ± s.d. of 3 independent replicates; one-way ANOVA with Tukey's multiple-comparisons test; $^{****}P < 0.0001$. **i**, Immunofluorescence of β4 integrin (green) and F-actin (magenta) in hSIOs enclosed in Matrigel–HCC–gelatin hydrogels at day 2, 5 and 8 of cell culture. Dashed lines indicate the hydrogel position. Scale bar, 25 μm. **j**, Representative bright-field and fluorescence images showing live (green, calcein stained) and dead (red, ethidium homodimer-1 stained) cells in hSIO cultures 2 d after Matrigel–HCC–8-arm PEG hydrogel photo-crosslinking. Scale bar, 400 μm. Inset shows a higher magnification of the organoid enclosed in the Matrigel–HCC–PEG hydrogel structure. Scale bar, 50 μm. $\Delta z = 300$ μm. Dashed lines indicate the position of the hydrogel. **k**, Representative images showing the morphology of a hSIO enclosed in HCC–PEG 3D-printed structures after 8 d in culture. Scale bar, 50 μm. **l**, Fluorescence imaging showing actin (magenta) localization and hydrogel localization of a hSIO enclosed by HCC–8-arm PEG 3D-printed structures after 8 d in culture. Nuclei were stained with Hoechst (blue). Scale bar, 50 μm. **m**, Feret's angle quantification of hSIOs enclosed by HCC–8-arm PEG (grey) or HCC–gelatin (black) 3 d and 6 d after hydrogel bioprinting. Data are shown as mean ± s.d. of five or six independent replicates; two-way ANOVA with Sidak's multiple-comparisons test. $^{****}P < 0.0001$. Specific bioprinting conditions are reported in Supplementary Table 5.

the effect of cell-laden i3D bioprinting on donor cells. The mCherry⁺ fibroblasts suspended in HCC–gelatin solution were injected under the epimysium (no i3D bioprinting) or injected and subjected to i3D bioprinting to generate parallelepiped-shaped constructs. Donor mCherry⁺ fibroblasts were identified in host animals 21 d after delivery in both experimental conditions (Supplementary Fig. 30b–h). However, imaging analysis showed elongated clusters of mCherry⁺ fibroblasts only in the mice in which i3D bioprinting had been performed, arranged along the anteroposterior axis of the parallelepiped-shaped constructs defined during i3D bioprinting (Supplementary Fig. 30b–e). Conversely, injected cells that were not i3D bioprinted were organized into rounded clusters (Supplementary Fig. 30b,f–h). We also performed i3D bioprinting across the epidermis; we observed elongated localization of mCherry⁺ fibroblasts 14 d after intradermal injection and i3D bioprinting of embedded donor cells into parallelepiped-shaped constructs, whereas injected, but not i3D bioprinted mCherry⁺ fibroblasts remained localized in rounded clusters (Supplementary Fig. 30i). These results strongly suggested that i3D bioprinting can elicit a desired spatial organization of delivered cells.

Intravital 3D bioprinting for de novo tissue formation. Finally, we aimed to demonstrate that i3D bioprinting has the potential to support de novo tissue formation. As a tissue model, we used skeletal muscle, since its formation requires anisotropic cell alignment during the early stages of skeletal muscle regeneration[44–46].

Many stem cells have been shown to possess myogenic potential and thus have been applied for cell therapy-based regenerative medicine approaches aimed at promoting skeletal muscle regeneration[45]. In particular, MuSCs can give rise to a large number of progeny able to contribute extensively to the formation of new muscle fibres when transplanted in vivo[44–46]. Moreover, MuSCs have the

HCC–gelatin hydrogels can be fabricated into pre-existing 3D environments and are suitable for 3D in vitro hSIo culture

objects fabricated in a drop of Matrigel

A human small intestinal organoid in Matrigel, enclosed by HCC–gelatin structures after hydrogel photo-crosslinking

Hydrogel was deformed by the organoid

basal localization of β4 integrin observed in hSIOs enclosed in HCC–gelatin structures suggests that cell adhesion could be a possible mechanism involved in the observed phenotype.

HCC– 8-arm PEG–Matrigel allowed hSIO survival and growth

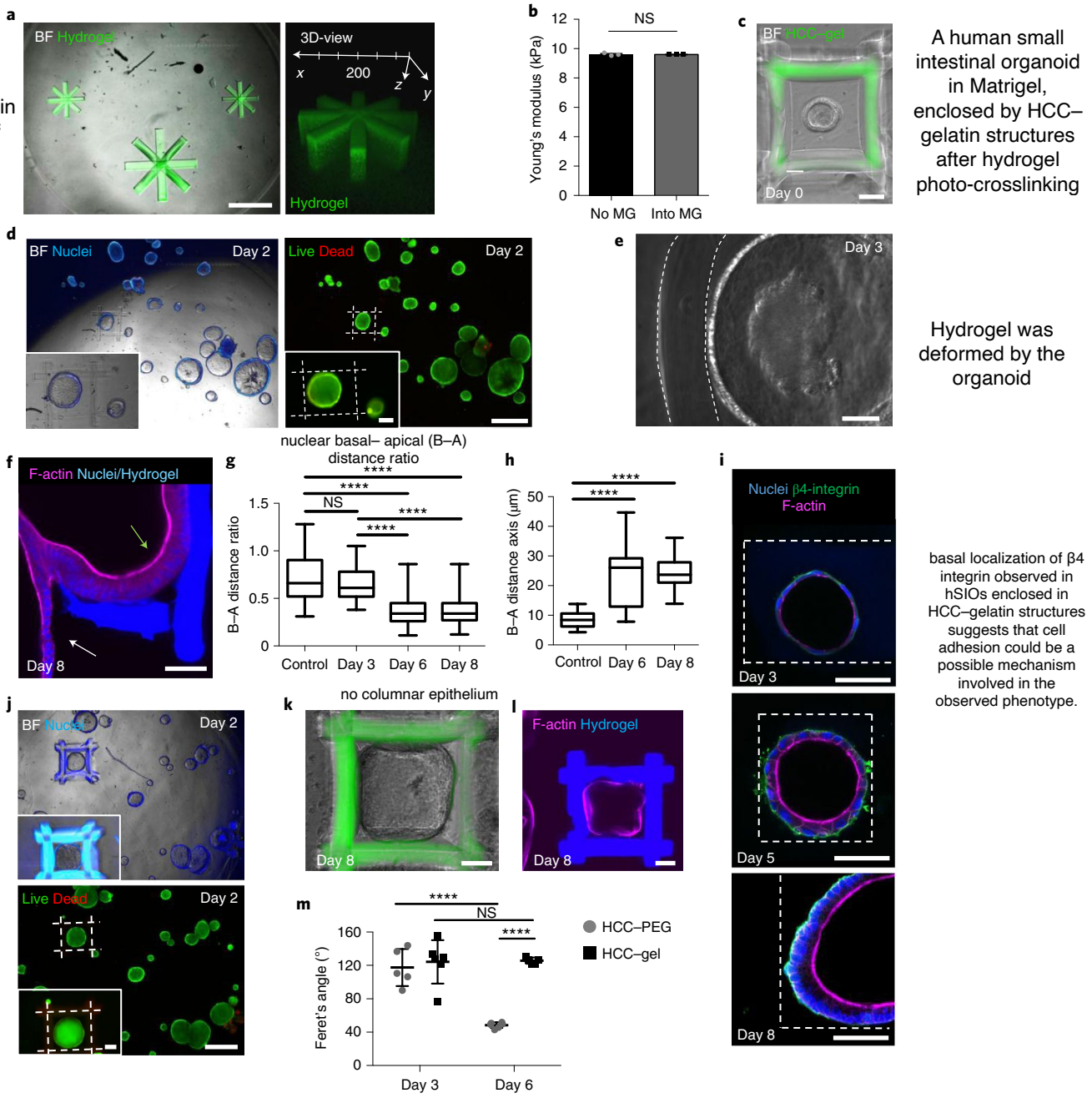

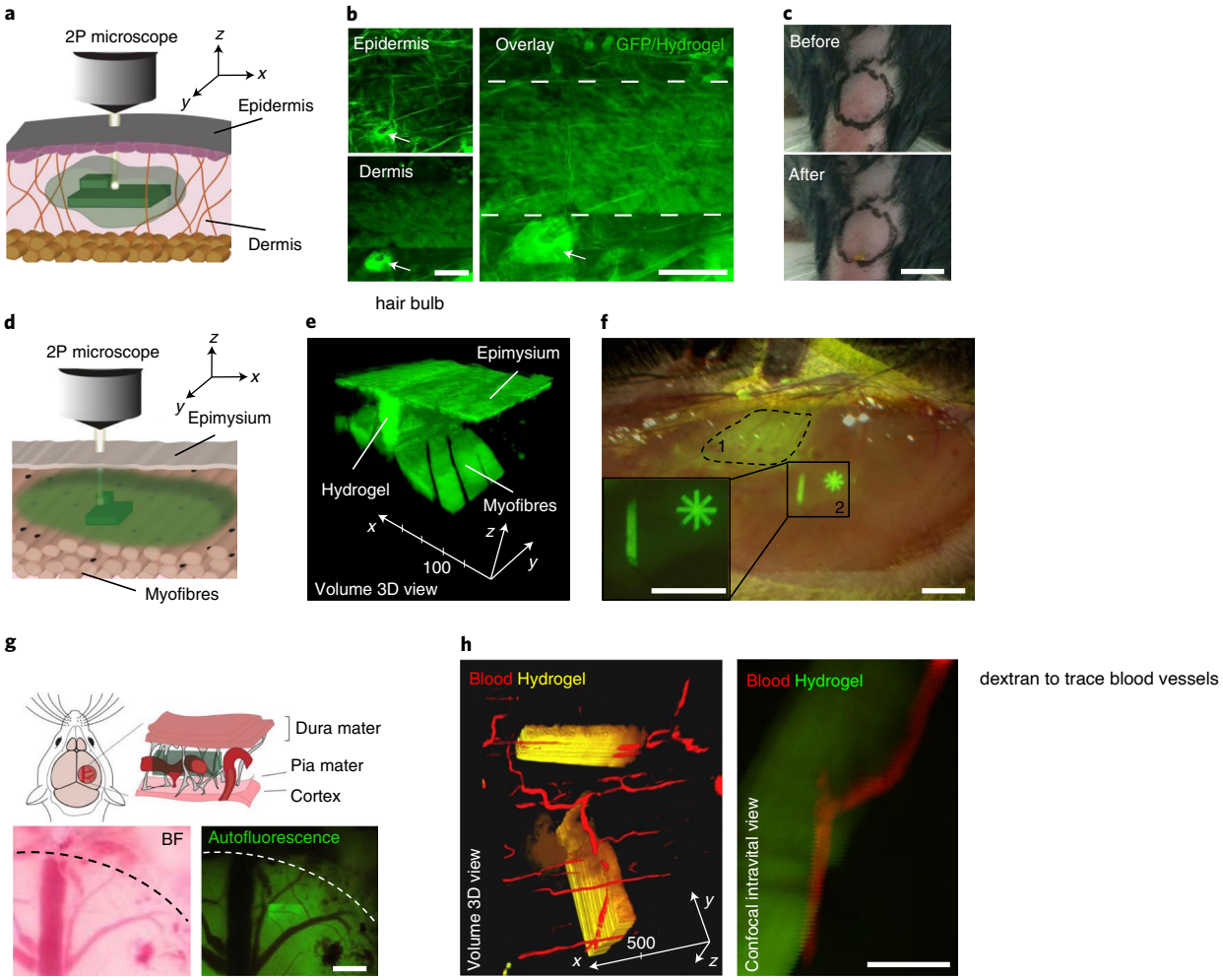

Fig. 6 | Intravital 3D bioprinting. a, Schematic showing two-photon crosslinking of HCC–hydrogel into dermis across the epidermis. **b**, Representative intravital imaging of 6 independent replicates, demonstrating integrity of epithelial cells of the epidermis and the HCC–8-arm PEG object fabricated into the dermis (green; $\Delta z = 100\,\mu m$) of the skin in GFP$^+$ mice. The dotted line in the overlay panel shows the margins of the hydrogel; arrow marks the hair bulb. Scale bars, 100 µm. **c**, Representative images of six independent replicates of hindlimb skin before and after i3D bioprinting across epidermis. Scale bar, 0.5 cm. **d**, Schematic showing two-photon crosslinking of HCC–hydrogel into skeletal muscle across epimysium. **e**, Representative 3D-volume reconstruction of 6 independent replicates showing HCC–8-arm PEG structure ($\Delta z = 300\,\mu m$) manufactured between undamaged myofibres and epimysium of skeletal muscle in GFP$^+$ mice; coordinates and 50 µm scale bar are shown. **f**, Bright-field and fluorescence stereomicroscope image showing injected HCC–gelatin under epimysium without (dotted line, 1) or with (continuous line, 2) hydrogel photo-crosslinking. The inset shows a higher magnification of the fabricated structures. Scale bars, 1 mm. **g**, Illustration and representative stereomicroscope images of 4 independent replicates showing a HCC–8-arm PEG object (green, $\Delta z = 500\,\mu m$) fabricated between dura and pia mater in the brain of wild-type mice. Dotted line shows the margins of the burr hole preformed into the skull. Scale bar, 850 µm. **h**, Left: representative 3D-volume reconstruction of 6 independent replicates showing HCC–8-arm PEG structures (yellow, $\Delta z = 300\,\mu m$) positioned at 90° to each other and fabricated across epimysium of skeletal muscle in wild-type mice. The integrity of the blood flow is shown in red. Right: representative confocal intravital image showing blood-flow persistence in the microvasculature embedded into the photo-crosslinked hydrogel across epimysium. Scale bar, 100 µm. Specific bioprinting conditions are reported in Supplementary Table 6.

ability to regenerate skeletal muscle when embedded in situ into a photo-crosslinked hydrogel to repair volumetric muscle damage[47]. However, the differentiation of MuSCs and maturation of myotubes into aligned myofibres follows restricted spatially defined patterns[35,36]. Since fibroblasts have been shown to support and sustain skeletal muscle regeneration[48–50], we designed an experimental strategy in which HCC–gelatin solution laden with both fibroblasts and MuSCs was used to test whether i3D bioprinting of parallelepipeds could promote de novo skeletal muscle formation. A defined ratio[51] of GFP$^+$ MuSCs to mCherry$^+$ in HCC–gelatin solution was injected and then i3D bioprinted into multiple parallelepiped-shaped constructs (Fig. 7a). As controls, mice were also injected with cells resuspended in PBS, or in Matrigel or HCC–gelatin solution without two-photon irradiation (Fig. 7a and Supplementary Fig. 31a–c). One week after treatments, confined bundle of elongated GFP$^+$ cells was observed only in mice that underwent i3D bioprinting (Fig. 7a,b). Conversely, after injection without i3D bioprinting, the host tissue contained sparse cells and randomly organized myotubes (Fig. 7b and Supplementary Fig. 31a–c). The bundles of elongated GFP$^+$ cells were integrated by the host tissue, with a functional three-dimensionally organized vascular network that was observed only in the i3D bioprinted mice (Fig. 7b). In agreement with the earlier results, quantification of cell directionality showed that i3D bioprinting enables spatially controlled cell engraftment (Fig. 7c). Immunofluorescence analysis confirmed that de novo formed tissue (GFP$^+$) comprises regenerating myofibres expressing

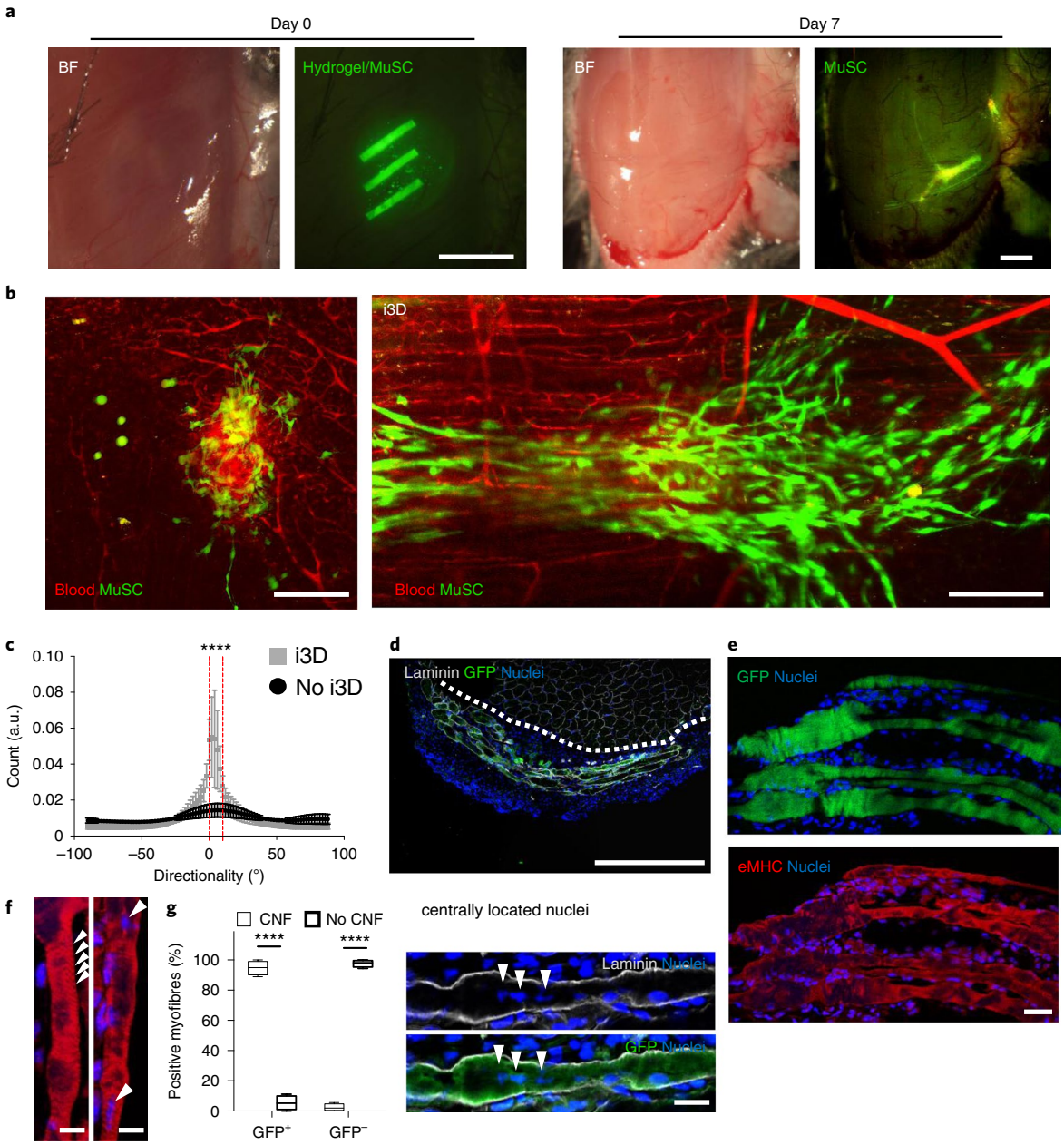

Fig. 7 | Cell-laden i3D bioprinting. a, Representative stereomicroscope images of independent replicates, showing hindlimb muscle just after (day 0) or 7 d after i3D bioprinting across epimysium of parallelepiped-shaped GFP+ MuSC and mCherry+ fibroblast HCC–gelatin constructs (green) into wild-type mice. Scale bar, 1 mm. **b**, Intravital two-photon mosaic image showing GFP+ MuSC-derived cells 7 d after injection under the epimysium (no i3D) or 7 d after injection and fabrication of parallelepiped-shaped GFP+ MuSC- (green) and mCherry+ fibroblast-laden HCC–gelatin construct (i3D) into wild-type mice. Blood flow is shown in red. Scale bar, 200 µm. **c**, Quantification of cell directionality of GFP+ cells in i3D bioprinted muscles (grey) or in muscles injected with GFP+ MuSC (black). Data are shown as mean ± s.d. of 4 independent replicates; one-way ANOVA with Tukey's multiple comparisons test; ****$P < 0.0001$. Specific bioprinting conditions are reported in Supplementary Table 6. **d**, Mosaic images showing host and de novo tissue sections. Immunofluorescence performed for GFP (green) and laminin (grey) in wild-type mice 7 d after i3D bioprinting of GFP+ MuSC- and mCherry+ fibroblast-laden HCC–gelatin. Dotted line shows the boundary between host muscle (above) and de novo tissue (below); scale bar, 400 µm. Nuclei were stained with Hoechst (blue). **e**, Confocal images of regenerating myofibres stained for GFP (green) and embryonic myosin heavy chain (eMHC; red). Scale bars, 30 µm. Nuclei were stained with Hoechst (blue). **f**, Higher magnification of regenerating myofibres stained for eMHC (red). Arrowheads point at striated organization of the cytoskeleton (left) and centrally located nuclei (right); scale bar, 15 µm. Nuclei were stained with Hoechst (blue). **g**, Left: quantification of GFP− and GFP+ myofibres, showing centrally located nuclei (CNF) or peripheral location of the nuclei (no CNF). Data are shown as mean ± s.d. of 4 independent replicates; two-way ANOVA with Sidak's multiple comparisons test. ****$P < 0.001$. Right: representative confocal image of four independent replicates showing a single multinucleated GFP+ myofibre surrounded by laminin; centrally located nuclei are highlighted by arrowheads. Scale bar, 10 µm. Nuclei were stained with Hoechst (blue).

embryonic myosin heavy chain protein and revealed striated organization of the muscular cytoskeleton and the presence of some centrally nucleated myofibres (Fig. 7d–f). Moreover, mCherry+ fibroblasts were found at the periphery of GFP+ myofibres derived from donor GFP+ MuSCs (Supplementary Fig. 31d). Immunostaining for GFP, laminin and nuclei was used to quantify

centrally nucleated myofibres. The analysis revealed that donor myofibres are mostly centrally nucleated. Conversely, host myofibres do not exhibit centrally located nuclei (Fig. 7g). Together, these results indicate that i3D bioprinting supports de novo skeletal muscle tissue formation, which is characterized by proper structural organization and integration with the host vascular system.

Outlook

We have shown that i3D bioprinting enables the fabrication of hydrogels that support the maintenance of cell functionality. With this approach, bioprinting is possible both in vitro to pre-existing 3D environments (Matrigel) and across tissues in different target organs in live animals, together with real-time imaging.

By allowing hydrogel fabrication in pre-existing 3D environments, i3D bioprinting technology could be used to advance our understanding of in vitro organoid models. Deliberate regulation of self-organization and morphogenesis has the potential to improve organoid topology and reproducibility, as well as to dissect mechanotransduction and biochemical mechanisms underpinning specific cell responses in 3D culture conditions[52]. Furthermore, we envision i3D bioprinting as a means to perform in vivo 3D confined cell delivery, capable of instructing cell structural organization within tissues. This strategy could improve the engraftment of cells after injection within tissues, avoiding fast dispersion and the short life-time of cells that typically occurs with this delivery strategy[53].

Moreover, i3D technology offers the opportunity to study cell biology and physiology in 3D environments, in which the internal structure and organization can be modified according to biological needs both in vitro and in vivo. We should underline that this approach could suffer from limitations related to multiphoton microscopy, such as the size and depth of hydrogel crosslinking at millimetre scales. Conversely, research in multi-photon microscopy and lithography is rapidly developing strategies to overcome such limitations[54], including deep tissue penetration with three-photon excitation[55], optical fibre guidance[56] and multiphoton holographic technology[57,58]. i3D bioprinting is currently limited to anatomical sites that can be exposed to the light source. However, we envision that in future i3D bioprinting may be coupled with emerging optical-imaging-guided surgery[59,60], with applications in minimally invasive surgical techniques suitable for tissue repair and reconstruction, and de novo tissue fabrication.

Methods

Animals. All procedures performed on animals were approved by the Ethics Committee of the University of Padova and authorized by the Italian Ministry of Health, animal licence no. 601/2017-PR. We performed experiments in four- to six-month-old wild-type mice of both female and male inbred C57BL/6 J strain and in transgenic C57BL/6-(ACTB-EGFP)/J mice. Mice were housed in individual cages in an environmentally controlled room (23 °C, 12 h:12 h light:dark cycle) and provided food and water ad libitum. For in vivo studies, the number of mice used ranged from four to six per experimental condition.

Chemicals. Two kilodalton methoxy PEG amine (mPEG-NH_2), 10 kDa 4-arm PEG amine pentaerythritol core (4-arm-PEG-NH_2), 20 kDa 8-arm PEG amine tripentaerythritol core (8-arm-PEG-NH_2) were obtained from Jenkem Technology. HCCA and EHCC were purchased from TCI Chemicals. Gelatin from porcine skin (gelatin, type A, 300 bloom, cell culture tested), CMMC, HC, HMC, HTMC, AMCAA, *N*-hydroxysuccinimide (NHS), *N*,*N*′-dicyclohexylcarbodiimide (DCC), triethylamine (TEA), 2,4,6-trinitrobenzensulfonic acid (TNBS), 3-aminopropyltriethoxysilane (APTES), Dulbecco's phosphate buffered saline without calcium and magnesium chloride (PBS), anhydrous dimethylsulfoxide (DMSO), diethyl ether, absolute ethanol, deuterated chloroform ($CDCl_3$), deuterated DMSO (DMSO-d_6), acetonitrile and trifluoroacetic acid were purchased from Sigma-Aldrich. Water for the preparation of all solutions was 'ultrapure' water (Milli-Q, 0.06 µS cm^{-1}) produced with a Millipore Milli-Q purification system. Salts and buffers were purchased from Fluka Analytical and Sigma-Aldrich[61,62].

Synthesis of linear HCC–PEG, HCC–4-arm PEG and HCC–8-arm PEG. HCCA (1.00 g, 4.85 mmol) was dissolved in anhydrous DMSO (20 ml), then NHS (1.12 g, 9.70 mmol) and DCC (2.00 g, 9.70 mmol) were added to the solution. The reaction mixture was stirred overnight in the dark and filtered to remove the insoluble dicyclohexylurea. The HCCA–NHS was isolated by precipitation in diethyl ether (450 ml). HCCA–NHS was washed with diethyl ether (30 ml × 3) and finally desiccated under vacuum. mPEG–NH_2 (1.00 g, 0.50 mmol) was dissolved in anhydrous DMSO (10 ml), then triethylamine (69.69 µl, 0.50 mmol) and HCCA–NHS (0.30 g, 1.00 mmol) were added to the solution. 4-arm PEG–NH_2 (1.00 g, 0.10 mmol) was dissolved in anhydrous DMSO (10 ml) and added to triethylamine (55.75 µl, 0.40 mmol) and HCCA–NHS (0.24 g, 0.80 mmol). The 8-arm PEG–NH_2 (1.00 g, 0.05 mmol) was dissolved in anhydrous DMSO (10 ml) and added of triethylamine (55.75 µl, 0.40 mmol) and HCCA–NHS (0.42 g, 1.40 mmol). After 12 h of stirring at room temperature in the dark, the reaction mixtures were added dropwise to diethyl ether (300 ml). HCCA–NHS was conjugated through an amide bond to polymers. The precipitates were recovered by centrifugation at 1,950*g* and dried under vacuum. The crude products were dissolved in a 9:1 (v/v) Milli-Q water/DMSO mixture and dialysed using Spectra/Por dialysis membranes (SpectrumLabs; molecular weight (MW) cut-off: 1 kDa, 3.5 kDa and 12–14 kDa for HCC–PEG, HCC–4-arm PEG and HCC–8-arm PEG, respectively). The dialysis was performed for 48 h using the same Milli-Q water/DMSO mixture as releasing medium and for 4 h using only Milli-Q water. Finally, the solutions were freeze dried, and the HCC-conjugated polymers were obtained as yellow solids (HCC–PEG yield: 0.82 g, 75%; HCC–4-arm PEG yield: 1.05 g, 91%; HCC–8-arm PEG yield: 0.99 g, 93%).

Synthesis of HCC–gelatin conjugate. HCCA (100 mg, 0.49 mmol) was dissolved in anhydrous DMSO (2 ml), then NHS (112 mg, 0.97 mmol) and DCC (200 mg, 0.97 mmol) were added to the solution. The reaction mixture was stirred overnight in the dark and filtered to remove the insoluble dicyclohexylurea. The 7-hydroxycoumarin-3-carboxylic acid *N*-succinimidyl ester (HCCA–NHS) was isolated by precipitation in diethyl ether (45 ml). The precipitate was rinsed with diethyl ether (30 ml × 3) and finally desiccated under vacuum. Gelatin (1.00 g, 0.01 mmol) was dissolved in anhydrous DMSO (30 ml) at 50 °C, then triethylamine (22.30 µl, 0.16 mmol) and HCCA–NHS (49 mg, 0.16 mmol) were added to the solution. HCCA–NHS was conjugated through an amide bond to gelatin. After 12 h stirring at 50 °C in the dark, the reaction mixture was diluted with 50 mM phosphate, pH 7.4 (120 ml) and dialysed with a Spectra/Por dialysis membrane (SpectrumLabs; MW cut-off: 12–14 kDa). The dialysis was performed for 36 h using a 9:1 (v/v) 50 mM phosphate/DMSO mixture as releasing medium and for 4 h using only Milli-Q water. Finally, the solution was freeze-dried, and the HCC–gelatin conjugate was obtained as yellow solid (yield: 0.99 g, 96%).

Synthesis of CMMC–4-arm PEG and CMMC–gelatin conjugate. CMMC (100 mg, 0.43 mmol) was dissolved in anhydrous DMSO (2 ml), then NHS (98 mg, 0.85 mmol) and DCC (176 mg, 0.85 mmol) were added. The reaction mixture was stirred overnight in the dark and filtered to remove the insoluble dicyclohexylurea. The CMMC–NHS was isolated by precipitation in diethyl ether (45 ml). The precipitate was rinsed with diethyl ether (30 ml × 3) and finally desiccated under vacuum.

For PEG conjugation, 10 kDa 4-arm PEG amine pentaerythritol core (4-arm PEG-NH_2, 1.0 g, 0.10 mmol) was dissolved in anhydrous DMSO (10 ml), then the reaction mixture was added of triethylamine (55.75 µl, 0.40 mmol) and CMMC–NHS (0.27 g, 0.80 mmol). CMMC–NHS was conjugated through an amide bond to polymers. After 12 h stirring at room temperature in the dark, the reaction mixtures were added dropwise to diethyl ether (300 ml). The precipitates were recovered by centrifugation at 4,000 rpm and dried under vacuum. The crude products were dissolved in a 9:1 (v/v) water/DMSO mixture and dialysed using Spectra/Por dialysis membranes (MW cut-off: 3.5 kDa, 12–14 kDa for CMMC–4-arm PEG and CMMC–8-arm PEG, respectively). The dialysis was performed for 48 h using the same water/DMSO mixture as releasing medium and for 4 h using only water. Finally, the solutions were freeze-dried, and the CMMC-conjugated polymers were obtained as solids (CMMC–4-arm PEG yield: 1.02 g, 94%). For gelatin conjugation, gelatin (1.00 g, 0.01 mmol) was dissolved in anhydrous DMSO (30 ml) at 50 °C, then triethylamine (22.30 µl, 0.16 mmol) and CMMC–NHS (53 mg, 0.16 mmol) were added to the solution. CMMC–NHS was conjugated through an amide bond to gelatin. After 12 h stirring at 50 °C in the dark, the reaction mixture was diluted with 50 mM phosphate, pH 7.4 (120 ml) and dialysed with a Spectra/Por dialysis membrane (SpectrumLabs; MW cut-off: 12–14 kDa). The dialysis was performed for 36 h using a 9:1 (v/v) 50 mM phosphate/DMSO mixture as releasing medium and for 4 h using only Milli-Q water. Finally, the solution was freeze-dried, and the CMMC–gelatin conjugate was obtained as white solid (yield: 0.95 g, 92%).

HCC–4-arm PEG, HCC–8-arm PEG and HCC–gelatin two-photon hydrogel crosslinking. HCC–4-arm PEG and HCC–8-arm PEG were dissolved in PBS (300 mg ml^{-1}) at room temperature under agitation. HCC–gelatin was dissolved in PBS (100 mg ml^{-1}) under agitation at 60 °C for 10 min. When coverslips were used, a second coverslip was placed on top of the drop of HCC-polymeric solutions to limit water evaporation during the irradiation process. For crosslinking reaction analysis, HCC–gelatin solution was prepared at the following concentrations, 100 mg ml^{-1}, 120 mg ml^{-1}, 140 mg ml^{-1}, 160 mg ml^{-1}, 180 mg ml^{-1} and 200 mg ml^{-1}.

HCC–gelatin or HCC–8-arm PEG were also mixed in a 50/50 ratio with Matrigel. Two-photon hydrogel crosslinking was achieved by using Scientifica 2-Photon microscope. Specific working conditions are reported in Supplementary Tables 3–6. Laser power is measured before objective back aperture, corresponding to about 1% of the power on the sample plane. In a typical working condition, standard line scan velocity was 0.8 mm ms^{-1}, pixel dwell time 2 µs and z spacing 1 µm. The time required to polymerize a volume of 1 mm^3 is about 30 min.

CMMC–4-arm PEG and CMMC–gelatin UV-mediated hydrogel crosslinking. For crosslinking reaction analysis, 5 µl of CMMC–4-arm PEG (300 mg ml^{-1}) or of CMMC–gelatin (100 mg ml^{-1}) solution was located in a humid chamber at 3 cm from a 365 nm UV light-emitting diode (LED) Gen 2 Emitter LZ4–04UV00 (Led Engin) and irradiated for different minutes as reported. When CMMC–gelatin solution was analysed at different concentrations (100 mg ml^{-1}, 120 mg ml^{-1}, 140 mg ml^{-1}, 160 mg ml^{-1}, 180 mg ml^{-1} and 200 mg ml^{-1}), 5 µl of solution was located in a humid chamber at 3 cm from a 365 nm UV LED Gen 2 Emitter LZ4-04UV00 (Led Engin) and irradiated for 3 min.

Cell cultures. HUVECs were transduced with a lentiviral vector encoding for eGFP[63] and cultured in endothelial growth medium (EGM, Lonza). For 2D culture on hydrogel, 20×10^4 cells were seeded onto HCC–gelatin structures (fabrication details reported in Supplementary Table 4), located in a 12-well culture dish and cultured for 24 h at 37 °C and 5% CO_2 in cell incubator.

NSC–neural progenitor cell (NPC) cultures were derived from hESCs. In brief, hESCs were detached using dispase and plated in low-adhesion dishes to generate embryoid bodies (EB) in the presence of two small molecules, SB-431542 (10 µM) and dorsomorphin (DSO, 3 µM), which inhibit TGF-β and BMP respectively, and ROCK inhibitor (10 µM, Miltenyi Biotec). After 5 d in culture, EBs were collected and plated on Matrigel-coated dishes in EB medium supplemented with DSO (1 µM) and FGF2 (10 ng ml^{-1}) to obtain neural rosettes. On day 6 EB medium was changed to N2 medium with DSO and FGF2 and changed daily until neural rosettes were formed. On day 12 after seeding, neural rosettes were picked and grown in suspension for 2 d in N2 medium with FGF2 (20 ng ml^{-1}). Finally, on day 14, floating rosettes were collected, digested with 0,025% Trypsin–EDTA and plated on tissue culture dishes coated with poly-ornithine–laminin in N2 medium with FGF2 (10 ng ml^{-1}), EGF (10 ng ml^{-1}) and B27 supplement (1:1,000) to obtain a NSC–NPC line. Cells were split with 0,025% Trypsin–EDTA every 3 d at 1:2 or 1:3 ratio. EB medium: DMEM/F-12 (Thermofisher, 11320-033), KnockOut Serum Replacement 20% (Thermofisher), β-mercaptoethanol (1:1,000; Gibco), non-essential amino acids (1:100; Gibco), L-glutamine 1:100 (Thermofisher Scientific, 25030024). N2 medium: DMEM/F-12 (Thermofisher, 11320-033), N-2 supplement 1% (Thermofisher) and D-glucose (350 µl per 100 ml; Thermofisher). For 2D culture on hydrogel, 3.2×10^5 cells were seeded onto HCC–gelatin structures (fabrication details reported in Supplementary Table 4), located in a 12-well culture dish and cultured for 3 d at 37 °C and 5% CO_2 in a cell incubator. After culture, cells were fixed in 4% (w/v) paraformaldehyde (Sigma-Aldrich) in PBS for 7 min at room temperature and maintained at 4 °C in PBS until use.

Primary muscular fibroblasts were isolated from wild-type or transgenic C57BL/6-(ACTB-EGFP)/J mice as previously described[64]. Following three passages of expansion, cells were transduced with a lentiviral vector encoding for mCherry[63]. After two passages, mCherry$^+$ fibroblasts were purified by fluorescence activated cell sorting on a BD FACS Aria IIIu, on the basis of the epifluorescence signal. Only mCherry$^+$ fibroblasts were collected and further expanded. For 3D cell-laden culture, 10^4 cells were seeded into Matrigel, or Matrigel or CMMC–gelatin exposed to UV light for 3 min at an irradiation distance of 3 mm, located in a 24-well culture dish, cultured for 2 d at 37 °C and 5% CO_2 in cell incubator before performing cell viability assay as described above. For two-photon cell-laden HCC–gelatin 3D bioprinting, 4×10^4 mCherry$^+$ fibroblasts or wild-type fibroblasts were resuspended in 10 µl of HCC–gelatin solution, drop cast on glass coverslip and processed as described in Supplementary Table 4. Two-photon cell-laden constructs were analysed by imaging or AFM as described above.

MuSCs were isolated from wild-type or transgenic C57BL/6-(ACTB-EGFP)/J mice as previously described[64]. Cells were expanded for one passage at 37 °C in cell incubator, using proliferating medium composed of DMEM supplemented with 20% horse serum, 10% foetal bovine serum (Gibco), 1% chicken embryo extract (Sera Laboratories International), bFGF (25 ng µl^{-1}; Invitrogen, PHG0264) and 1% penicillin/streptomycin (Thermofisher). For two-photon cell-laden 3D bioprinting, 2×10^4 MuSCs were resuspended in 5 µl of HCC–gelatin solution, drop cast on glass coverslip and processed as described in Supplementary Table 4. For 3D cell-laden culture, 1×10^4 cells were seeded into Matrigel, or CMMC–gelatin exposed to UV light for 3 min at an irradiation distance of 3 mm. Samples were located in a 24-well culture dish, cultured for 2 d at 37 °C and 5% CO_2 in cell incubator before performing cell viability assay as described above. For two-photon cell-laden HCC–gelatin 3D bioprinting, 2×10^4 MuSCs were resuspended in 10 µl of HCC–gelatin solution, drop cast on a glass coverslip and processed as described in Supplementary Table 4. Samples were cultured in proliferating media and analysed 2 d after 3D bioprinting (cell directionality was quantified as reported above). For long-term 3D culture, 2×10^4 cells were seeded onto 3D elongated HCC–gelatin two-photon crosslinked hydrogels (as described in Supplementary Table 4). After 5 d of culture in proliferating medium, differentiation medium (DMEM supplemented with 2% horse serum and 1% penicillin/streptomycin) was used for the following 5 d of cell culture. After 10 d, samples were fixed in 4% (w/v) paraformaldehyde (Sigma-Aldrich) in PBS for 7 min at room temperature and maintained at 4 °C in PBS until use.

Human small intestinal crypt stem cells were isolated from a small intestine paediatric biopsy following a well-established dissociation protocol[65,66]. Isolated crypts were cultured in pure Matrigel growth factor reduced (BD 354230) droplets and expanded in WENR medium of a base AdDMEM + ++:Advanced DMEM F-12 (Thermo 12634),10 mM HEPES (Thermo 15630080), 2 mM Glutamax (Thermo 35050061), 1% penicillin/streptomycin (Thermo 15140122) supplemented with B-27 supplement minus vitamin A (Thermo 12587010), 1.25 mM *N*-acetylcysteine (Sigma A9165), penicillin/streptomycin (Thermo 15140122), 100 ng ml^{-1} Wnt-3A (Peprotech 315-20), 500 ng ml^{-1} R-spondin 1 (Peprotech 120-38), 100 ng ml^{-1} Noggin (R&D 6057-NG), 50 ng ml^{-1} EGF (Thermo PMG8043), 10 nM Gastrin (Sigma G9020), 3 µM GSK-3 inhibitor (CHIR 99021) (Tocris 4423), 500 nM TGF-β inhibitor (A83-01) (Sigma SML0788), 10 µM p38 inhibitor (SB202190) (Sigma S7067), 10 nM prostaglandin E2 (Cambridge, cay14010). When indicated, small intestinal enteroids were transfected with lentiviral vector for GFP$^+$. Enteroids were passaged every 6–8 d with 5 min TrypLE (Thermo 12605010) dissociation and seeded in new Matrigel droplets. For the multiphoton experiments, hSIOs that were recently passaged (1–2 d) were washed thoroughly from the old Matrigel with cold AdDMEM + ++. Cells were pelleted at 400 g and surnatant discarded. For HCC–gelatin/Matrigel 50/50 experiments, HCC–gelatin 10% solution was melted at 60 °C for 5 min and quickly mixed 1:1 to liquid Matrigel at 4 °C to form a pre–gel with final concentration of 5% HCC–gelatin and 50% Matrigel. Cell pellet was quickly resuspended in the pre-gel mixture and the droplets were allowed to solidify for 15 min at 37 °C, before proceeding to two-photon crosslinking (as described in Supplementary Table 5). After two-photon printing, samples were cultured for 2, 3, 6 or 8 d in the above WENR medium before being used for analysis. For basal–apical distance ratio[67] and basal–apical major axis[66], measurements were performed on confocal fluorescence images stained for nuclei and actin by using ImageJ software (Feret's angle was quantified as reported above).

Intravital HCC–4-arm PEG, HCC–8-arm PEG, HCC–gelatin 3D printing and intravital HCC–gelatin bioprinting. Mice were anaesthetized using intraperitoneal injection of Zoletil 50/50 (40 mg kg^{-1}) and Rompun 2% Xilazina (5 mg kg^{-1}) in physiologic solution. Induction of deep surgical anaesthesia was confirmed by absence of reaction to hindfoot pinch. The surgical procedure underwent in aseptic conditions (skin preparation, sterilized instruments, gloves and drapes). Photosensitive polymers were either autoclaved (HCC–4-arm PEG or HCC–8-arm PEG) or 0.22 µm filtered (HCC–gelatin) before in vivo application. Specific working conditions used for i3D bioprinting are described in Supplementary Table 6. For blood-flow analysis, rhodamine B isothiocyanate–dextran (Sigma, R9379) was injected into the tail vein at 50 mg ml^{-1} in physiologic solution. When required, the skin wound was closed with Vicryl 6–0 suture and no movement or space restriction was applied to mice after treatments. At the required time point, mice were deeply anaesthetized, subjected to stereomicroscope and/or two-photon intravital imaging, then sacrificed for tissue collection.

For i3D printing into skin, intra-dermal injection of 20 µl of HCC–4-arm PEG or HCC–8-arm PEG solutions (300 mg ml^{-1} in PBS) was performed at the abdomen, ear or hindlimb using insulin syringes (Sacco, MED320924). Defined regions of interest were subject to two-photon irradiation across the epidermis for hydrogel crosslinking and mice were analysed after i3D bioprinting.

For i3D printing into muscle, a skin incision was performed to expose the epimysium of the lateral hindlimb. Then, 10 µl of HCC–4-arm PEG or HCC–8-arm PEG solution (300 mg ml^{-1} in PBS) was injected between the epimysium and the skeletal muscle using insulin syringes (Sacco, MED320924). Defined regions of interest were subject to two-photon irradiation for hydrogel crosslinking between the epimysium and myofibres and mice were analysed after i3D bioprinting, 4 h or 4 d after treatment.

For i3D printing into brain, a skin incision was performed to expose the skull. A small window in the skull (approximately 3 mm in diameter) was made with a drill around the bregma to expose the brain. Then, 4 µl of HCC–8-arm PEG solution (300 mg ml^{-1} in PBS) was injected sub-meningeally using a Hamilton syringe connected to a glass capillary. For all the procedure, a glass coverslip was located above the site of the injection to allow objective immersion in PBS, before proceeding to i3D printing and intravital imaging.

For i3D bioprinting of mCherry$^+$ fibroblasts, 1.4×10^4 cells were resuspended in 8 µl of HCC–gelatin and then injected sub-epidermally or between the epimysium and the skeletal muscle by using insulin syringes, then eventually processed for i3D bioprinting and analysed 14 or 21 d after treatment.

For i3D bioprinting of muscular cells, a mix of 1.4×10^4 GFP$^+$ MuSCs and 6×10^3 mCherry$^+$ fibroblasts were used (70:30) (ref. [51]) were resuspended in 8 µl of HCC–gelatin, PBS or Matrigel and then injected between the epimysium and the skeletal muscle of wild-type mice using insulin syringes, then eventually processed for i3D bioprinting. All mice were analysed 7 d after treatment.

Image preparation and analysis. We used ImageJ software for adjustments of levels and contrast, maximum and standard deviation intensity projections, 3D reconstructions and thresholding to create binary masks used for directionality and Feret's angle measurements. To quantify the directionality of i3D bioprinted cells, at least nine fluorescence images of independent biological triplicates for each sample were converted in binary masks, then analysed with directionality plugin of ImageJ software (which indicates the amount of structures in a given direction). To quantify the shape of enclosed hSIOs, at least nine fluorescence images of independent biological triplicates for each sample were converted in binary masks, then analysed with measure plugin of ImageJ software to quantify the Feret's angle (the angle between the longest distance of the axis of any two points along the selection boundary (Feret's diameter) and a line parallel to the *x*-axis of the image). All mentioned ImageJ plugins have source code available and are licensed under open-source GNU GPL v.3 license.

Statistical analysis. All analyses were performed with GraphPad prism 6. We expressed data as mean ± s.e.m or mean ± s.d of multiple biological replicates (as indicated in the figure legend). We determined statistical significance by unequal variance Student's *t*-test, one-way analysis of variance (ANOVA) and Tukey's multiple comparison test or two-way ANOVA and Sidak's multiple comparisons test. A *P* value of less than 0.05 was considered statistically significant.

Reporting Summary. Further information on research design is available in the Nature Research Reporting Summary linked to this article.

Data availability

The main data supporting the results in this study are available within the paper and its Supplementary Information. The raw image data and the analysed data generated in this study are available from the corresponding author upon reasonable request.

Received: 22 July 2019; Accepted: 8 May 2020;
Published online: 22 June 2020

References

1. Kruth, J. P. Material incress manufacturing by rapid prototyping techniques. *CIRP Ann. Manuf. Technol.* **40**, 603–614 (1991).
2. Gross, B. C., Erkal, J. L., Lockwood, S. Y., Chen, C. & Spence, D. M. Evaluation of 3D printing and its potential impact on biotechnology and the chemical sciences. *Anal. Chem.* **86**, 3240–3253 (2014).
3. Moroni, L. et al. Biofabrication strategies for 3D in vitro models and regenerative medicine. *Nat. Rev. Mater.* **3**, 21–37 (2018).
4. Murphy, S. V. & Atala, A. 3D bioprinting of tissues and organs. *Nat. Biotechnol.* **32**, 773–785 (2014).
5. Ong, C. S. et al. 3D bioprinting using stem cells. *Pediatr. Res.* **83**, 223–231 (2018).
6. Kang, H. W. et al. A 3D bioprinting system to produce human-scale tissue constructs with structural integrity. *Nat. Biotechnol.* **34**, 312–319 (2016).
7. Hong, N., Yang, G.-H., Lee, J. & Kim, G. 3D bioprinting and its in vivo applications. *J. Biomed. Mater. Res. B* **106**, 444–459 (2018).
8. Wang, M. et al. The trend towards in vivo bioprinting. *Int. J. Bioprint.* **1**, 15–26 (2015).
9. Skardal, A. et al. Bioprinted amniotic fluid-derived stem cells accelerate healing of large skin wounds. *Stem Cells Transl. Med.* **1**, 792–802 (2012).
10. Binder, K. W. et al. In situ bioprinting of the skin for burns. *J. Am. Coll. Surg.* **211**, S76 (2010).
11. Keriquel, V. et al. In situ printing of mesenchymal stromal cells, by laser-assisted bioprinting, for in vivo bone regeneration applications. *Sci. Rep.* **7**, 1–10 (2017).
12. Di Bella, C. et al. In situ handheld three-dimensional bioprinting for cartilage regeneration. *J. Tissue Eng. Regen. Med* **12**, 611–621 (2018).
13. Wang, X., Rivera-Bolanos, N., Jiang, B. & Ameer, G. A. Advanced functional biomaterials for stem cell delivery in regenerative engineering and medicine. *Adv. Funct. Mater.* **29**, 1–31 (2019).
14. Zhang, Z., Wang, B., Hui, D., Qiu, J. & Wang, S. 3D bioprinting of soft materials-based regenerative vascular structures and tissues. *Composites B* **123**, 279–291 (2017).
15. Chin, S. Y. et al. Additive manufacturing of hydrogel-based materials for next-generation implantable medical devices. *Sci. Robot.* **2**, eaah6451 (2017).
16. Murphy, S. V., Skardal, A. & Atala, A. Evaluation of hydrogels for bio-printing applications. *J. Biomed. Mater. Res. A* **101**, 272–284 (2013).
17. König, K. Multiphoton microscopy in life sciences. *J. Microsc.* **200**, 83–104 (2000).
18. Chang, H., Shi, M., Sun, Y. & Jiang, J. Photo-dimerization characteristics of coumarin pendants within amphiphilic random copolymer micelles. *Chin. J. Polym. Sci.* **33**, 1086–1095 (2015).
19. Mahon, M. F., Raithby, P. R. & Sparkes, H. A. Investigation of the factors favouring solid state [2+2] cycloaddition reactions; the [2+2] cycloaddition reaction of coumarin-3-carboxylic acid. *CrystEngComm* **10**, 573–576 (2008).
20. Wang, D., Hou, X., Ma, B., Sun, Y. & Wang, J. UV and NIR dual-responsive self-assembly systems based on a novel coumarin derivative surfactant. *Soft Matter* **13**, 6700–6708 (2017).
21. Belfield, K. D., Bondar, M. V., Liu, Y. & Przhonska, O. V. Photophysical and photochemical properties of 5,7-di- methoxycoumarin under one- and two-photon excitation. *J. Phys. Org. Chem.* **16**, 69–78 (2002).
22. Iliopoulos, K., Krupka, O., Gindre, D. & Salle, M. Reversible two-photon optical data storage in coumarin-based copolymers. *J. Am. Chem. Soc.* **132**, 14343–14345 (2010).
23. Kim, S. H., Sun, Y., Kaplan, J. A., Grinstaff, M. W. & Parquette, J. R. Photo-crosslinking of a self-assembled coumarin-dipeptide hydrogel. *N. J. Chem.* **39**, 3225–3228 (2015).
24. Kabb, C. P., O'Bryan, C. S., Deng, C. C., Angelini, T. E. & Sumerlin, B. S. Photoreversible covalent hydrogels for soft-matter additive manufacturing. *ACS Appl. Mater. Interfaces* **10**, 16793–16801 (2018).
25. Zhu, C. & Bettinger, C. J. Light-induced remodeling of physically crosslinked hydrogels using near-IR wavelengths. *J. Mater. Chem. B* **2**, 1613–1618 (2014).
26. Azagarsamy, M. A., McKinnon, D. D., Alge, D. L. & Anseth, K. S. Coumarin-based photodegradable hydrogel: design, synthesis, gelation, and degradation kinetics. *ACS Macro Lett.* **3**, 515–519 (2014).
27. Williams, C. G., Malik, A. N., Kim, T. K., Manson, P. N. & Elisseeff, J. H. Variable cytocompatibility of six cell lines with photoinitiators used for polymerizing hydrogels and cell encapsulation. *Biomaterials* **26**, 1211–1218 (2005).
28. Torgersen, J. et al. Hydrogels for two-photon polymerization: A toolbox for mimicking the extracellular matrix. *Adv. Funct. Mater.* **23**, 4542–4554 (2013).
29. Xing, J.-F., Zheng, M.-L. & Duan, X.-M. Two-photon polymerization microfabrication of hydrogels: an advanced 3D printing technology for tissue engineering and drug delivery. *Chem. Soc. Rev.* **44**, 5031–5039 (2015).
30. Ingber, D. E. Cellular mechanotransduction: putting all the pieces together again. *FASEB J.* **20**, 811–827 (2006).
31. Dupont, S. et al. Role of YAP/TAZ in mechanotransduction. *Nature* **474**, 179–184 (2011).
32. Bian, L. et al. The influence of hyaluronic acid hydrogel crosslinking density and macromolecular diffusivity on human MSC chondrogenesis and hypertrophy. *Biomaterials* **34**, 413–421 (2013).
33. Brigo, L. et al. 3D high-resolution two-photon crosslinked hydrogel structures for biological studies. *Acta Biomater.* **55**, 373–384 (2017).
34. Lefort, C. A review of biomedical multiphoton microscopy and its laser sources. *J. Phys. D* **50**, 423001 (2017).
35. Ostrovidov, S. et al. Skeletal muscle tissue engineering: methods to form skeletal myotubes and their applications. *Tissue Eng. B* **20**, 403–436 (2014).
36. Moon, D. G., Christ, G., Stitzel, J. D., Atala, A. & Yoo, J J. Cyclic mechanical preconditioning improves engineered muscle contraction. *Tissue Eng. A* **14**, 473–482 (2008).
37. Gjorevski, N. et al. Designer matrices for intestinal stem cell and organoid culture. *Nature* **539**, 560–564 (2016).
38. Morra, M. On the molecular basis of fouling resistance. *J. Biomater. Sci. Polym. Ed.* **11**, 547–569 (2000).
39. Drumheller, P. D. & Hubbell, J. A. J. Densely crosslinked polymer networks of poly(ethylene glycol) in trimethylolpropane triacrylate for cell-adhesion-resistant surfaces. *Biomed. Mater. Res.* **29**, 207–215 (1995).
40. Gjorevski, N. & Lutolf, M. P. Synthesis and characterization of well-defined hydrogel matrices and their application to intestinal stem cell and organoid culture. *Nat. Protoc.* **12**, 2263–2274 (2017).
41. Kominami, K. et al. The molecular mechanism of apoptosis upon caspase-8 activation: quantitative experimental validation of a mathematical model. *Biochim. Biophys. Acta* **1823**, 1825–1840 (2012).
42. Tummers, B. & Green, D. R. Caspase-8; regulating life and death. *Immunol. Rev.* **277**, 76–89 (2017).
43. Swartzlander, M. D., Lynn, A. D., Blakney, A. K., Kyriakides, T. R. & Bryant, S. J. Understanding the host response to cell-laden poly(ethylene glycol)-based hydrogels. *Biomaterials* **34**, 952–964 (2013).
44. Qazi, T. H. et al. Cell therapy to improve regeneration of skeletal muscle injuries. *J. Cachexia Sarcopenia Muscle* **10**, 501–516 (2019).
45. Yin, H., Price, F. & Rudnicki, M. A. Satellite cells and the muscle stem cell niche. *Physiol. Rev.* **93**, 23–67 (2013).
46. Cerletti, M. et al. Highly efficient, functional engraftment of skeletal muscle stem cells in dystrophic muscles. *Cell* **134**, 37–47 (2008).
47. Rossi, C. A. et al. In vivo tissue engineering of functional skeletal muscle by freshly isolated satellite cells embedded in a photopolymerizable hydrogel. *FASEB J.* **25**, 2296–2304 (2011).
48. Chapman, M. A., Meza, R. & Lieber, R. L. Skeletal muscle fibroblasts in health and disease. *Differentiation* **92**, 108–115 (2016).
49. Mendias, C. L. Fibroblasts take the centre stage in human skeletal muscle regeneration. *J. Physiol.* **595**, 5005 (2017).

50. Murphy, M. M., Lawson, J. A., Mathew, S. J., Hutcheson, D. A. & Kardon, G. Satellite cells, connective tissue fibroblasts and their interactions are crucial for muscle regeneration. *Development* **138**, 3625–3637 (2011).
51. Urciuolo, A. et al. Decellularised skeletal muscles allow functional muscle regeneration by promoting host cell migration. *Sci. Rep.* **8**, 8398 (2018).
52. Rossi, G., Manfrin, A. & Lutolf, M. P. Progress and potential in organoid research. *Nat. Rev. Genet.* **19**, 671–687 (2018).
53. Foster, A. A., Marquardt, L. M. & Heilshorn, S. C. The diverse roles of hydrogel mechanics in injectable stem cell transplantation. *Curr. Opin. Chem. Eng.* **15**, 15–23 (2017).
54. Hoover, E. E. & Squier, J. A. Advances in multiphoton microscopy technology. *Nat. Photonics* **7**, 93–101 (2013).
55. Horton, N. G. et al. In vivo three-photon microscopy of subcortical structures within an intact mouse brain. *Nat. Photonics* **7**, 205–209 (2013).
56. Delrot, P., Loterie, D., Psaltis, D. & Moser, C. Single-photon three-dimensional microfabrication through a multimode optical fiber. *Opt. Express* **26**, 1766–1778 (2018).
57. Chu, W. et al. Centimeter-height 3D printing with femtosecond laser two-photon polymerization. *Adv. Mater. Technol.* **3**, 1700396 (2018).
58. Schultz, S. R., Copeland, C. S., Foust, A. J., Quicke, P. & Schuck, R. Advances in two-photon scanning and scanless microscopy technologies for functional neural circuit imaging. *Proc. IEEE Inst. Electr. Electron. Eng.* **105**, 139–157 (2017).
59. Horváth, O. P. Minimal invasive surgery. *Acta Chir. Hung.* **36**, 130–131 (1997).
60. Palep, J. H. Robotic assisted minimally invasive surgery. *J. Minim. Access Surg.* **5**, 1–7 (2009).
61. Sims, G. E. C. & Snape, T. J. A method for the estimation of polyethylene glycol in plasma protein fractions. *Anal. Biochem.* **107**, 60–63 (1980).
62. Habeeb, A. F. S. A. Determination of free amino groups in proteins by trinitrobenzenesulfonic acid. *Anal. Biochem.* **14**, 328–336 (1966).
63. Natarajan, D. et al. Lentiviral labeling of mouse and human enteric nervous system stem cells for regenerative medicine studies. *Neurogastroenterol. Motil.* **26**, 1513–1518 (2014).
64. Urcuiolo, A. et al. Collagen VI regulates satellite cell self-renewal and muscle regeneration. *Nat. Commun.* **4**, 1964 (2013).
65. Jung, P. et al. Isolation and in vitro expansion of human colonic stem cells. *Nat. Med.* **17**, 1225–1227 (2011).
66. Sato, T. et al. Long-term expansion of epithelial organoids from human colon, adenoma, adenocarcinoma, and Barrett's epithelium. *Gastroenterology* **141**, 1762–1772 (2011).
67. Ajduk, A., Biswas Shivhare, S. & Zernicka-Goetz, M. The basal position of nuclei is one pre-requisite for asymmetric cell divisions in the early mouse embryo. *Dev. Biol.* **392**, 133–140 (2014).

Acknowledgements

This work was supported by 2017 STARS-WiC grant of University of Padova, Progetti di Eccellenza CaRiPaRo, TWINING of University of Padova, Oak Foundation Award (grant no. W1095/OCAY-14-191), 'Consorzio per la Ricerca Sanitaria' (CORIS) of the Veneto Region, Italy (LifeLab Program) to N.E. and the STARS Starting Grant 2017 of University of Padova (grant code LS3-19613) to A.U. P.D.C. is supported by the National Institute for Health Research (NIHR; grant no. NIHR-RP-2014-04-046). G.G.G. was supported by the NIHR Great Ormond Street Hospital Biomedical Research Centre Catalyst Fellowship. G.G.G., P.D.C. and N.E. were supported by the Oak award W1095/OCAY-14-191. All research at Great Ormond Street Hospital NHS Foundation Trust and University College London Great Ormond Street Institute of Child Health is made possible by the NIHR Great Ormond Street Hospital Biomedical Research Centre. The views expressed are those of the author(s) and not necessarily those of the National Health Service, the NIHR or the Department of Health. We thank D. Moulding for technical support and S. Schiaffino for scientific advice and discussion.

Author contributions

A.U. and N.E. designed the experiments. N.E. designed the photochemistry, I.P. synthesized and chemically characterized the coumarin polymers and S.S. contributed to the chemical characterization of coumarin polymers. A.U. performed and analysed in vitro and in vivo experiments. L.Brandolino. and P.R. contributed to in vitro experiments. V.S. contributed to the analysis of in vivo experiments. C.L. performed hydrogel injection into the brain and derived reporter cells and human ES cell-derived NSCs. G.G.G., E.Z., G.S. and M.M. contributed to organoid experiments. G.G. and P.D.C. characterized human intestinal organoid cultures. L.Brigo. contributed to the design and interpretation of in vitro two-photon crosslinking experiments. M.G. performed AFM analysis. A.U. and N.E. analysed the data and wrote the manuscript. N.E. supervised the project.

Competing interests

N.E. has an equity stake in ONYEL Biotech s.r.l. A.U. and N.E. are submitting a patent for the intravital 3D bioprinting (provisional patent number 102020000008779).

Additional information

Supplementary information is available for this paper at https://doi.org/10.1038/s41551-020-0568-z.

Correspondence and requests for materials should be addressed to N.E.

Reprints and permissions information is available at www.nature.com/reprints.

Publisher's note Springer Nature remains neutral with regard to jurisdictional claims in published maps and institutional affiliations.

nature research

Corresponding author(s): Nicola Elvassore

Last updated by author(s): May 1, 2020

Reporting Summary

Nature Research wishes to improve the reproducibility of the work that we publish. This form provides structure for consistency and transparency in reporting. For further information on Nature Research policies, see Authors & Referees and the Editorial Policy Checklist.

Statistics

For all statistical analyses, confirm that the following items are present in the figure legend, table legend, main text, or Methods section.

n/a	Confirmed	
☐	☒	The exact sample size (*n*) for each experimental group/condition, given as a discrete number and unit of measurement
☐	☒	A statement on whether measurements were taken from distinct samples or whether the same sample was measured repeatedly
☐	☒	The statistical test(s) used AND whether they are one- or two-sided *Only common tests should be described solely by name; describe more complex techniques in the Methods section.*
☐	☒	A description of all covariates tested
☐	☒	A description of any assumptions or corrections, such as tests of normality and adjustment for multiple comparisons
☐	☒	A full description of the statistical parameters including central tendency (e.g. means) or other basic estimates (e.g. regression coefficient) AND variation (e.g. standard deviation) or associated estimates of uncertainty (e.g. confidence intervals)
☐	☒	For null hypothesis testing, the test statistic (e.g. *F*, *t*, *r*) with confidence intervals, effect sizes, degrees of freedom and *P* value noted *Give P values as exact values whenever suitable.*
☒	☐	For Bayesian analysis, information on the choice of priors and Markov chain Monte Carlo settings
☒	☐	For hierarchical and complex designs, identification of the appropriate level for tests and full reporting of outcomes
☒	☐	Estimates of effect sizes (e.g. Cohen's *d*, Pearson's *r*), indicating how they were calculated

Our web collection on statistics for biologists contains articles on many of the points above.

Software and code

Policy information about availability of computer code

Data collection	For the multiphoton imaging acquisition and for 3D intavital bioprinting Scientifica Sci.scan software was used. For confocal-imaging acquisition, Leica LAS AF or Zeiss ZEN Imaging software were used. Customized User Environment (CUE) software was used for absorption-spectra acquisition.
Data analysis	For graph preparation and statistical analysis Prism 6 was used. NMR data were processed with MestreNova 6.2.0 software. ImageJ software was used for adjustments of levels and contrast, maximum and standard deviation intensity projections, 3D reconstructions (https://imagej.net/3D_Viewer) and thresholding to create binary mask used for directionality (https://imagej.net/Directionality) and ferret angle (https://imagej.nih.gov/ij/docs/guide/146-30.html) measurements.

For manuscripts utilizing custom algorithms or software that are central to the research but not yet described in published literature, software must be made available to editors/reviewers. We strongly encourage code deposition in a community repository (e.g. GitHub). See the Nature Research guidelines for submitting code & software for further information.

Data

Policy information about availability of data

All manuscripts must include a data availability statement. This statement should provide the following information, where applicable:

- Accession codes, unique identifiers, or web links for publicly available datasets
- A list of figures that have associated raw data
- A description of any restrictions on data availability

The main data supporting the results in this study are available within the paper and its Supplementary Information. The raw image data and the analysed data generated in this study are available from the corresponding author on reasonable request.

Field-specific reporting

Please select the one below that is the best fit for your research. If you are not sure, read the appropriate sections before making your selection.

☒ Life sciences ☐ Behavioural & social sciences ☐ Ecological, evolutionary & environmental sciences

For a reference copy of the document with all sections, see nature.com/documents/nr-reporting-summary-flat.pdf

Life sciences study design

All studies must disclose on these points even when the disclosure is negative.

Sample size	For the in vivo studies, the number of animals used ranged from 4 to 6 per each experimental condition. For the in vitro studies, at least 3 biological independent replicates were used, and 3 technical replicates of each were analysed.
Data exclusions	No data were excluded from the analyses.
Replication	Experiments were replicated within our laboratory, and independently across laboratories and Universities.
Randomization	Not applicable.
Blinding	For the ex vivo characterization and quantification, the investigators were blinded to the samples and control samples that they were analysing. For the in vitro and in vivo experiments, a blind approach was not possible since the hydrogel fabrication was visible.

Reporting for specific materials, systems and methods

We require information from authors about some types of materials, experimental systems and methods used in many studies. Here, indicate whether each material, system or method listed is relevant to your study. If you are not sure if a list item applies to your research, read the appropriate section before selecting a response.

Materials & experimental systems

n/a	Involved in the study
☐	☒ Antibodies
☐	☒ Eukaryotic cell lines
☒	☐ Palaeontology
☐	☒ Animals and other organisms
☒	☐ Human research participants
☒	☐ Clinical data

Methods

n/a	Involved in the study
☒	☐ ChIP-seq
☒	☐ Flow cytometry
☒	☐ MRI-based neuroimaging

Antibodies

Antibodies used	The following primary antibodies were used: 1:100 Rat anti-α-Laminin (Sigma, L0663), 1:50 Rabbit anti-GFP (Invitrogen, A11122), 1:25 Mouse anti-eMyHC (DSHB, F1.652-s), 1:100 Rabbit anti-F4/80 (Santa Cruz Biotechnology, sc-25830), 1:25 Rabbit anti-MyoG (Santa Cruz Biotechnology, sc-576), 1:100 Rabbit anti-Human Ezrin (Thermo, PA5-29358); 1:100 Rat anti-integrin beta-4 (Abcam, ab110167); 1:50 Mouse anti-PEG (GenScript, 5E10E9); 1:500 Mouse anti-hNestin (Millipore, MAB 5326); 1:5000 Mouse anti-BIII-Tubulin (Tuj1 – Biolegend, 801202); 1:50 Goat anti-Sox1 (R&D, AF3369); 1:200 Rabbit anti-Pax6 (Biolegend, 901301); 1:2000 Rabbit anti-p75 (Promega, G323A); 1:1000 Goat anti-GFAP (Abcam, ab53554); 1:10 Goat anti-collagen I (SouthernBiotech, 1310-01); 1:50 Rabbit anti-caspase-8 p18 (H-134; Sigma, sc-7890). The following secondary antibodies were used: 1:200 Donkey anti-mouse 488 (ThermoFisher, A21202); 1:200 Donkey anti-rabbit 488 (ThermoFisher, A21206); 1:200 Donkey anti-mouse 594 (ThermoFisher, A21203); 1:200 Donkey anti-rabbit 594 (ThermoFisher, A31573); 1:500 Goat anti-mouse 594 (ThermoFisher R37121); 1:500 Goat anti-Rabbit 568 (ThermoFisher, A-11011); 10 µg/mL Hoechst 33342 (ThermoFisher, H1399); 1:100 Goat anti-Rat Cy2 (Jackson, 112-225-167).
Validation	All the antibodies were validated on proper ex vivo and/or in vitro samples.

Eukaryotic cell lines

Policy information about cell lines

Cell line source(s)	HUVECs; human embryonic stem cells H9 were used to derive neural stem cells. Murine primary muscular fibroblasts and muscle stem-cell-derived cells were derived from wild-type or transgenic C57BL/6-(ACTB-EGFP)/J mice. Human small intestinal crypt stem cells were isolated from a small intestine pediatric biopsy.
Authentication	Cells were characterized by using specific markers.

Mycoplasma contamination	The cell lines tested negative for mycoplasma contamination.
Commonly misidentified lines (See ICLAC register)	No commonly misidentified cell lines were used.

Animals and other organisms

Policy information about studies involving animals; ARRIVE guidelines recommended for reporting animal research

Laboratory animals	We performed experiments in wild-type inbred C57BL/6J mice and in transgenic C57BL/6-(ACTB-EGFP)/J mice, 4–6 months old (female and male).
Wild animals	The study did not involved wild animals.
Field-collected samples	The study did not involve samples collected from the field.
Ethics oversight	All the animal procedures were approved by the Ethics Committee of the University of Padova, and authorized by the Italian Ministry of Health (animal license n. 601/2017-PR).

Note that full information on the approval of the study protocol must also be provided in the manuscript.